Journal of Neuroinflammation

RESEARCH

Open Access

THBS1 in macrophage-derived exosomes exacerbates cerebral ischemia–reperfusion injury by inducing ferroptosis in endothelial cells

Chang Liu[1,2,3,4], Haijing Sui[2,5], Zhixi Li[2,3,4,5], Zhenyu Sun[2,5], Chenglong Li[6], Guangmin Chen[7], Zhaoxue Ma[2,5], Hang Cao[2,5] and Hongjie Xi[2,5*]

Abstract

Macrophages play a critical role in the development of acute ischemic stroke (AIS). Cerebral ischemia–reperfusion injury (CIRI) is a pivotal pathological process that exacerbates AIS, with exosomes act as crucial mediators. However, the effects and mechanisms of action of macrophage-derived exosomes on CIRI remain unclear. This study demonstrated that macrophage-derived exosomes induce endothelial ferroptosis and barrier disruption during CIRI. Through proteomic sequencing and the reanalysis of transcriptomic and single-cell sequencing data, thrombospondin-1 (THBS1) was identified as a key exosomal molecule. Elevated THBS1 was observed in exosomes and monocytes from the peripheral blood of patients with AIS in oxygen–glucose deprivation/reoxygenation (OGD/R)-stimulated THP-1 and RAW264.7, in their secreted exosomes, and in macrophages within the brains of transient middle cerebral artery occlusion (tMCAO) mice. Additionally, THBS1 expression in exosomes was positively correlated with vascular barrier injury biomarkers, including MMP-9 and S100B. Modulation of THBS1 in macrophage-derived exosomes affected exosome-induced ferroptosis in endothelial cells. The mechanism by which THBS1 binds directly to OTUD5 and promotes GPX4 ubiquitination was elucidated using RNA interference, adeno-associated virus transfection, and endothelial-specific Gpx4 knockout mice. High-throughput screening of small-molecule compounds targeting THBS1 was performed. Molecular docking, molecular dynamics simulations, and cellular thermal shift assays further confirmed that salvianolic acid B (SAB) has a potent binding affinity for THBS1. SAB treatment inhibited the interaction between THBS1 and OTUD5, leading to reduced GPX4 ubiquitination. Further research revealed that SAB treatment enhanced the cerebral protective effects of THBS1 inhibition. In conclusion, this study explored the role of exosome-mediated signaling between macrophages and cerebral vascular endothelial cells in CIRI, highlighting the THBS1-OTUD5-GPX4 axis as a driver of endothelial ferroptosis and brain injury. Targeting this signaling axis represents a potential therapeutic strategy for treating CIRI.

Keywords Ischemic stroke, Cerebral ischemia–reperfusion injury, Macrophage, Endothelial cells, Exosomes

*Correspondence:
Hongjie Xi
xihongjie@hrbmu.edu.cn
Full list of author information is available at the end of the article

Graphical Abstract

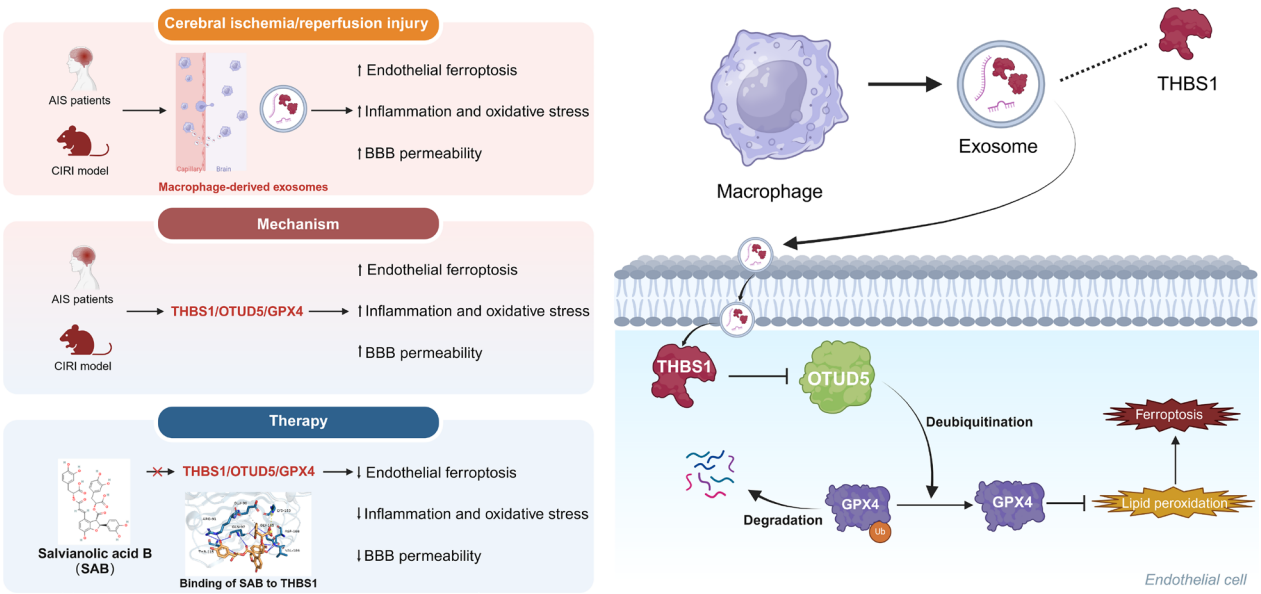

Introduction

Acute ischemic stroke (AIS), characterized by cerebral arterial occlusion, leads to an immediate energy crisis in brain tissue. The primary clinical approach for treating AIS is the early restoration of blood flow to the ischemic region to salvage tissue in the ischemic penumbra. However, reperfusion can induce secondary brain damage, referred to as cerebral ischemia–reperfusion injury (CIRI), which significantly influences patient prognosis. The pathophysiology of CIRI is complex, and despite notable advancements in treatment over recent years, disability and mortality rates remain high [1, 2]. Therefore, further exploration of the molecular mechanisms underlying CIRI and the search for novel therapeutic targets are essential for improving patient outcomes. The mechanisms underlying CIRI are complex, with blood–brain barrier (BBB) disruption serving as a pivotal factor in the pathological process. An intact BBB plays a selective filtering role, which is crucial for maintaining central nervous system homeostasis. Endothelial cells and tight junctions are vital for preserving the typical structure and function. During CIRI, endothelial structural damage and impaired barrier function provide a pathway for blood-borne substances to damage brain tissue during reperfusion [3–5]. Therefore, maintaining endothelial homeostasis and restoring endothelial barrier integrity are critical for CIRI treatment.

Ferroptosis is a distinct form of programmed cell death characterized by excessive production and accumulation of reactive oxygen species (ROS) and increased lipid peroxidation driven by iron overload [6, 7]. Glutathione peroxidase 4 (GPX4), a key regulator of ferroptosis, suppresses lipid peroxidation and maintains intracellular redox balance, thereby preventing the initiation and progression of the process [8]. In pathological conditions such as ischemia, reperfusion, and infection, cellular metabolism and molecular expression patterns are altered, and oxidative balance is disrupted, characterized by decreased GSH levels and increased ROS levels. These changes can interfere with the normal regulation of GPX4 through transcriptional control and post-translational modifications, leading to reduced expression, thereby increasing the cell's susceptibility to ferroptosis [8, 9]. Recent studies have demonstrated that endothelial cells are particularly sensitive to ferroptosis and show significantly elevated ferroptosis under oxygen–glucose deprivation/reoxygenation (OGD/R) conditions [10]. Our previous research and previous research of others indicate that inhibiting endothelial ferroptosis effectively alleviates CIRI and plays a crucial role in improving patient outcomes [11–13]. However, the regulatory mechanisms underlying ferroptosis in brain microvascular endothelial cells in CIRI remain unclear and require further investigation.

Various cell types contribute to the pathophysiology of CIRI through exosome secretion, with macrophages serving as a major source [14]. Macrophage infiltration increases in brain tissue during CIRI [15], and

exosomes from macrophages activated by hypoxic conditions impair endothelial cell viability [16], indicating exosome-mediated signaling as a critical communication mechanism between macrophages and endothelial cells. Furthermore, pro-inflammatory macrophage-derived exosomes induce mitochondrial dysfunction in endothelial cells and elevate intracellular ROS levels, processes closely associated with ferroptosis [17]. Studies have shown that pro-inflammatory macrophage-derived exosomes can induce ferroptosis in cells, including epithelial and tumor cells [18, 19]. Although increasing evidence suggests that macrophage-derived exosomes contribute to ferroptosis, their impact on brain microvascular endothelial cells during CIRI and the underlying mechanisms, as well as their potential role in mediating ferroptosis, remain unclear and require further investigation.

This study investigated the effects and mechanisms of macrophage-derived exosomes on cerebral vascular endothelial cells and brain tissue during CIRI. Our findings indicate that macrophages induce endothelial ferroptosis and barrier disruption via exosomal pathways during CIRI. Through proteomic sequencing, transcriptomic data analysis, single-cell sequencing, and experimental validation, thrombospondin-1 (THBS1) was identified as a key factor in this process. Mechanistically, THBS1 interacted with OTUD5 to promote GPX4 ubiquitination, thereby increasing the sensitivity of endothelial cells to ferroptosis and contributing to endothelial barrier disruption. Additionally, salvianolic acid B (SAB) was identified as a compound that effectively binds to THBS1, and SAB treatment potentiated the neuroprotective effects of THBS1 inhibition. This study revealed a novel pathological mechanism underlying cerebral vascular injury during CIRI and highlights the potential of targeting THBS1 as a therapeutic strategy for mitigating CIRI.

Materials and methods

Reagent

Mouse IL-6 and TNF-α, and human THBS1, MMP-9, and S100B ELISA kits were purchased from Jingkang (Shanghai, China). Salvianolic acid B (HY-N1362), ferrostatin-1 (HY-100579), and GW4869 (HY-19363) were purchased from MedChemExpress (NJ, USA). PMA (P1585) and PKH67 were purchased from Sigma (USA). Lipofectamine 2000 was purchased from Invitrogen (Carlsbad, CA, USA). DiR (UR21017) was purchased from UmiBio (Shanghai, China). Phalloidin (MX4405) was purchased from MkBio (Shanghai, China). Propidium iodide (PI), DAPI, Hoechst, JC-1, DHE, and ROS staining kits were purchased from Beyotime (Shanghai, China). Zombie NIR dye was obtained from BioLegend (CA, USA). CCK8 and Liperfluo were provided by DOJINDO (Kumamoto, Japan). AceQ qPCR SYBR Green Master Mix kit (Q111-03) was supplied by Vazyme (Nanjing, China). First-strand cDNA Synthesis Kit (FSK-101) was obtained from TOYOBO (Osaka, Japan).

Preparation and validation of animal models

Male C57BL/6 mice were purchased from the Animal Experiment Center of the Second Affiliated Hospital of Harbin Medical University and maintained under standardized conditions (25 ± 2 °C, 40–60% humidity, 12-h light/dark cycle) with ad libitum access to food and water. A cerebral ischemia–reperfusion injury (CIRI) model was established using the transient middle cerebral artery occlusion (tMCAO) method, as previously described [20]. The procedure was as follows: A midline neck incision was made, and the cervical glands and fascia were bluntly dissected to expose the common carotid artery (CCA), external carotid artery (ECA), and internal carotid artery (ICA). The ICA and its extracranial branches, including the pterygopalatine artery, were carefully isolated to avoid damage while ensuring ICA patency as the sole branch of the CCA. The ECA trunk was isolated, and its branches were electrocoagulated and ligated distally before transection. A "V"-shaped incision was created at the distal ECA using ophthalmic scissors. The CCA and ICA were temporarily clamped with microvascular clips. A heparin-coated nylon filament (602256PK5Re, Doccol) was inserted into the ECA and advanced into the ICA after removing the ICA clip until it occluded the middle cerebral artery (MCA) origin. Cerebral blood flow was monitored, with a 70–80% reduction in cortical blood flow indicating successful occlusion. The filament was secured at the ECA bifurcation with a suture, and the clamps on the CCA were removed. The incision was closed in layers. After 90 min of MCA occlusion, the filament was removed to allow reperfusion and cerebral blood flow was recorded again. Sham-operated mice underwent the same procedures, excluding filament insertion.

The administration of exo and drug

Exosomes derived from mouse macrophages were isolated by ultracentrifugation and resuspended in sterile PBS. Protein concentrations were determined using the BCA assay, and exosome samples were normalized to a uniform concentration. Exosome suspensions were injected via the tail vein at a dose of 5 μg/g, and their effects on mice were assessed at predefined time points. Based on previous study [21] of the ferroptosis-inhibitory effects and our preliminary experimental data, SAB was administered via tail vein injection at a dose of 15 mg/kg for five consecutive days. Two hours after the final

injection, the tMCAO model was induced, and various indicators were evaluated at corresponding time points.

Cell culture

Cell lines THP-1 and RAW264.7 were obtained from the Cell Bank of the Chinese Academy of Sciences (Shanghai, China), while human brain microvascular endothelial cells (HBMECs) were sourced from ScienCell. THP-1 cells were cultured in RPMI 1640 medium supplemented with 10% FBS, and RAW264.7 cells were maintained in DMEM with 10% FBS. HBMECs were cultured in ECM supplemented with 5% FBS and 1% endothelial growth supplement. With reference to previous literature [22, 23], HBMECs were co-cultured with exosomes (60 μg/mL) for 24 h, and changes were observed with or without ferrostatin-1 (2 μM) treatment, which was applied 2 h before co-culture. The concentration of SAB applied to HBMECs was 10 μM.

Construction of the OGD/R cell model

THP-1 cells were differentiated into macrophages by exposure to PMA (50 ng/mL) for 24 h before further experiments. The OGD/R macrophage model was established according to previously reported protocols [24]. Differentiated THP-1 and RAW264.7 cells were cultured in glucose-free DMEM at 37 °C under hypoxic conditions (1% O_2, 5% CO_2, 94% N_2) in a tri-gas incubator for 4 h. Subsequently, the medium was replaced with glucose-containing DMEM, and the cells were incubated under normoxic conditions (21% O_2, 5% CO_2, 74% N_2) at 37 °C for 24 h to induce reoxygenation.

Collection of conditioned medium and exosome enrichment and identification

The cell culture supernatant was collected and centrifuged at 2000 rpm for 10 min to remove cell debris. The supernatant was then filtered through a 0.22 μm filter to obtain conditioned medium.

For exosome isolation, supernatants from cells cultured with exosome-free fetal bovine serum (EVs-free FBS) were transferred into clean centrifuge tubes and centrifuged at 2000 × g for 20 min at 4 °C to remove cells and dead cells. The resulting supernatant was centrifuged at 10,000 × *g* for 30 min at 4 °C to eliminate any remaining debris, followed by further collection of the supernatant. The supernatant was ultracentrifuged at 120,000 × *g* for 70 min to pellet the crude exosomal fraction. The pellet was resuspended in cold PBS and centrifuged at 120,000 × *g* for 70 min. The supernatant was discarded, and the pellet was resuspended in an appropriate volume of cold PBS. The protein concentration was quantified using the BCA assay for further analysis.

Nanoparticle Tracking Analysis (NTA): Exosome samples were diluted in PBS for NTA. After automatic calibration of the instrument, the exosome samples were further diluted with sterile PBS to achieve a particle count between 50 and 400 within the detection interface, at which point measurements were initiated.

Transmission Electron Microscopy (TEM): A 10 μL drop of exosome suspension was placed onto a copper grid and left for 1 min. Uranyl acetate was added to the grid and incubated for another minute. After drying, the samples were imaged under an electron microscope at 100 kV.

Patient recruitment and sample collection

Healthy volunteers were recruited from the hospital staff through open-call advertisements. The inclusion criteria included the following: patients aged 18 to 85 years, National Institutes of Health Stroke Scale (NIHSS) score (8 to 25), time from symptoms onset to endovascular thrombectomy within 8 h, modified Rankin Scale (mRS) ≤ 1, and core infarct volume < 50 mL on magnetic resonance imaging or Alberta Stroke Program Early Computed Tomography Score (ASPECTS) ≥ 6. The key exclusion criteria included previous stroke within 30 days, unknown time of symptom onset, associated myocardial infarction or severe infection (sepsis or endocarditis), any known hemorrhagic or coagulation deficiency, and stenosis or any occlusion in a proximal vessel that prevented access to the site of occlusion. All patients were diagnosed at the Second Affiliated Hospital of Harbin Medical University and received antiplatelet therapy after admission. The baseline characteristics of AIS patients and healthy volunteers are summarized in Additional file 1: Table S1. Blood samples from 32 healthy volunteers and 56 AIS patients were collected, and peripheral PBMCs were isolated following the manufacturer's instructions.

TTC staining

Twenty-four hours after reperfusion, the mice were euthanized, and brain tissues were collected. The brains were frozen for 15 min, sectioned into 1-mm slices, and stained with 2% TTC solution at 37 °C for 15 min, with intermittent flipping to ensure uniform staining. Infarcted regions appeared white, whereas non-infarcted regions were stained red.

Evans blue staining

Mice were administered 0.5% Evans blue dye via tail vein injection at a dose of 2 mL/kg. After 30 min, the mice were euthanized, and brain tissues were harvested. Each brain sample was placed in a 1.5 mL centrifuge tube, followed by the addition of 1 mL of 50% trichloroacetic acid

(diluted with PBS). The tissue was rapidly homogenized using a tissue homogenizer and centrifuged at 10,000*g* for 20 min. The resulting supernatant was collected and diluted fourfold with absolute ethanol. Absorbance at 620 nm was measured using a spectrophotometer to determine the optical density (OD). The Evans blue concentration in the samples was then calculated based on the standard curve.

Measurement of brain water content

Mice were euthanized 24 h after reperfusion, and brain tissues were rapidly harvested. The tissues were dried at 100 °C for 48 h and weighed both before and after drying. Brain water content (%) was calculated using the following formula: Brain water content (%) = [(wet weight−dry weight)/wet weight] × 100%.

Adhesive removal test

The adhesive removal test was performed according to previous literature [25, 26]. The test was performed using a 2 × 3 mm tape. Adhesive tape was applied to the ipsilateral or contralateral forepaws of mice to evaluate their sensory and motor functions. Time was recorded when the mouse perceived the sticker attached to the foot and removed it as the time of contact and time of removal. The time to contact and time-to-remove the mouse were measured for up to 120 s.

Corner test

The corner test is a widely used functional assessment tool for unilateral sensorimotor cortical damage [27]. Two cardboard plates (30 × 20 cm) were attached at a 30° angle in the home cage. Each mouse was placed between the two plates and allowed to move freely toward the corners. The number of times the mice turned to the left over 10 trials was recorded. Only mice without a preference for turning left or right during the pre-training period were included. Normal mice make approximately equal numbers of left and right turns in their exploratory turning behavior. After ischemic and reperfusion insults to the sensorimotor cortex, mice showed biased turns consistent with the side of brain damage.

HE staining

Paraffin-embedded brain tissue sections were baked at 60 °C for 2 h, followed by standard deparaffinization with xylene and graded ethanol to water. The sections were stained with hematoxylin for 5 min, rinsed under running water, and counterstained with eosin, followed by another rinse. Finally, the sections were dehydrated, cleared, mounted, and imaged under a microscope.

Tunel staining

Paraffin-embedded brain tissue sections were baked at 60 °C for 2 h, followed by standard deparaffinization with xylene and graded ethanol to water. Each sample was incubated with 100 µL of Proteinase K working solution at room temperature for 20 min. The sections were washed three times with PBS for 5 min per wash. Equilibration Buffer was diluted 1:5 with ddH_2O, covering the sample area, and equilibrated at room temperature for 10–30 min. After discarding the buffer, 50 µL of TdT incubation buffer was applied, and the sections were incubated in a humid chamber at 37 °C for 60 min. Following three additional PBS washes, the sections were counterstained with DAPI. A final PBS wash was performed before mounting with anti-fade mounting medium. Fluorescence microscopy was used for observation.

DHE staining

Frozen brain tissue sections were thawed to room temperature and washed three times with PBS. The sections were incubated with a 10 µM dihydroethidium [28] fluorescent probe at 37 °C in the dark for 30 min. Following washing, the nuclei were counterstained with DAPI, and images were acquired using a fluorescence microscope.

Exosome tracing experiments

DiR dye working solution was prepared and added to the exosome suspension (100 µL of dye solution per 1000 µL of exosome suspension). The mixture was vortexed for 1 min and incubated at 37 °C for 30 min. After adding PBS, the solution was ultracentrifuged at 120,000 × *g* for 70 min to obtain the labeled exosomes. DiR-labeled exosomes were injected via the tail vein, and the mice were euthanized 6 h later. Brain tissue was harvested for ex vivo imaging to assess exosome distribution in the brain.

PKH67 dye was used for labeling. Mixture A was prepared by adding 50 µL of exosomes to 0.5 mL of Diluent C, while Mixture B was prepared by mixing 0.5 mL of Diluent C with 4 µL of PKH67. Mixtures A and B were then combined and incubated for 15 min. The staining reaction was stopped by adding 1 mL of 0.5% BSA. Labeled exosomes were obtained by ultracentrifugation and either co-cultured with HBMECs or injected via the tail vein. Confocal microscopy was used to examine the distribution of exosomes in cells or brain tissue sections.

Cell transfection

The siRNA was synthesized and purified by GenePharma. Transfection was conducted with 50 nM Lipofectamine™ 2000 when cell density reached 40–60%. Both siRNA and

transfection reagent were diluted in Opti-MEM and gently mixed by pipetting three to five times. The mixture was incubated at room temperature for 20 min and then slowly added dropwise to the culture medium. Following incubation in a CO_2 incubator for 4–6 h, the medium was replaced with fresh culture medium, and subsequent treatments were applied. Transfection efficiency was evaluated at 24–72 h after transfection. Specific small interfering RNA sequences are provided in Additional file 1: Table S2.

RT-qPCR

Trizol solution was added to the wells and incubated at room temperature for 10 min. Adherent cells were resuspended by gentle pipetting and transferred to nuclease-free centrifuge tubes. Chloroform was added and mixed thoroughly to extract RNA, followed by isopropanol to precipitate RNA from the supernatant. After centrifugation, the supernatant was discarded, and the pellet was washed with ethanol. The sample was centrifuged again, and the supernatant was removed. The RNA pellet was air-dried at room temperature and dissolved in an appropriate volume of nuclease-free water. RNA concentration was measured, and cDNA was synthesized using a reverse transcription kit. The PCR procedure was carried out according to the kit instructions. Detailed primer information is provided in Additional file 1: Table S3.

PI staining

The cell culture medium was replaced with staining buffer containing 5 μL of Hoechst reagent and 5 μL of PI reagent per milliliter. The cells were incubated at 4 °C for 30 min. Following PBS washes, images were acquired using a fluorescence microscope.

Liperfluo staining

The culture medium was removed, and the cells were washed once with serum-free medium. Liperfluo working solution was added, and the cells were incubated at 37 °C for 30 min. After removing the supernatant, the cells were washed twice with serum-free medium, and images were acquired using a confocal microscope.

JC-1 staining

JC-1 staining was performed to assess mitochondrial membrane potential. The JC-1 solution was diluted 1:200 in staining buffer and thoroughly mixed to prepare the working solution. Cells were incubated with the JC-1 working solution at 37 °C for 20 min. After incubation, the cells were washed with staining buffer and counterstained with Hoechst. Finally, images were acquired using a confocal microscope.

ROS staining

Intracellular reactive oxygen species (ROS) levels were measured using the fluorescent probe DCFH-DA. The probe was diluted to 10 μM in DMEM. The culture medium was replaced with the DCFH-DA working solution, and the cells were incubated at 37 °C for 30 min. After removing the probe, the cells were counterstained with Hoechst, and ROS levels were visualized using a fluorescence microscope.

Nissl staining

The paraffin-embedded mouse brain sections were dewaxed to water. The sections were then immersed in toluidine blue staining solution and incubated at 50–60 °C for 30 min. After a brief rinse with distilled water, rapid differentiation was performed using 95% ethanol. The sections were dehydrated with absolute ethanol, cleared with xylene, and mounted with neutral resin. The intensity of Nissl bodies in the cortical penumbra region of tMCAO mice (Sham group: cortex supplied by the left middle cerebral artery) was observed under a microscope to ensure consistency in imaging locations.

Western blot analysis

Protein samples were separated using sodium dodecyl sulfate–polyacrylamide gel electrophoresis. The gel was cut and transferred to a 0.22 μm PVDF membrane at 300 mA for 2 h under ice bath conditions. The membrane was blocked with 5% skim milk for 50 min and incubated with the primary antibody: ZO-1 (1:2000, AF5145, Affinity, OH, USA), Claudin5 (1:1000, E8F3D, Cell Signaling Technology, MA, USA), Occludin (1:1000, 91,131, Cell Signaling Technology, MA, USA), β-actin (1:100,000, AC026, ABclonal, Wuhan, China), GAPDH (1:2500, ab9485, Abcam, Cambridge, UK), SLC7A11 (1:10,000, ab175186, Abcam, Cambridge, UK), GPX4 (1:10,000, ab125066, Abcam, Cambridge, UK), Calnexin (1:2000, AF5362, Affinity, OA, USA), TSG101 (1:3000, DF8427, Affinity, OA, USA), CD81 (1:2000, DF2306, Affinity, OA, USA), CD63 (1:1000, AF5117, Affinity, OA, USA), THBS1 (1:2000, 18,304–1-AP, Proteintech, IL, USA), and Ub (1:2000, PTM-1107, Jingjie, Hangzhou, China). After washing with TBST, the membrane was incubated with secondary antibodies (1:10,000, ab6712, Abcam, Cambridge, UK; 1:100,000, AS003, ABclonal, Wuhan, China) for 1 h, followed by additional washing with TBST. Chemiluminescent imaging was performed using an ECL reagent.

Cellular thermal shift assay (CETSA)

The interaction between SAB and THBS1 was validated using a cellular thermal shift assay (CETSA). Cell lysates

treated with either vehicle or SAB were divided into ten equal aliquots and heated at temperatures ranging from 37 °C and 64 °C. After two freeze–thaw cycles with liquid nitrogen, the supernatant was collected for further analysis [29].

Virtual screening

The L6000 natural product library (L6000-Targetmol-Natural Product Library for HTS, 4320 compounds) from TopScience was used for virtual screening. The 2D structure data files (SDF) were imported into Schrödinger software, where the LigPrep module was employed to generate 3D structures for each compound using the OPLS_4 force field. The Epik module was used to calculate all possible stereoisomers and protonation states.

The docking grid center was positioned at the crystallized ligand in the small-molecule GDP-binding pocket. The outer box size was adjusted to accommodate the crystallized ligand, while the inner box size was set to 10 Å. Molecular docking was performed using Schrödinger's Virtual Screening Workflow module, with LigPrep-prepared 3D structures serving as the screening database.

The virtual screening process comprised four steps. (1) High-Throughput Virtual Screening (HTVS): All stereoisomeric states of each ligand were retained, with one conformer generated per stereoisomer. The top 50% of compounds based on scores were selected for further screening. [30] Standard Precision (SP): The highest-scoring stereoisomer of each ligand was retained, and one conformer per stereoisomer was generated. The top 20% of compounds were selected for the subsequent round. (3) Extra Precision (XP): Only the best-scoring stereoisomer of each ligand was retained, and one conformer was generated. The top 100 compounds were selected for further analyses. (4) MM-GBSA: Final compounds were rescored using binding free energy calculations, and compounds with MM-GBSA scores above -50 kcal/mol or duplicates were removed.

Molecular dynamics simulation

Molecular dynamics simulations were performed using Gromacs 2022.3. Plantainoside D (PD) was pre-processed with AmberTools22, employing the GAFF force field, and hydrogen atoms were added using Gaussian 16W to calculate the RESP charges, which were subsequently incorporated into the system's topology file. The simulations were conducted at a constant temperature of 300 K and a pressure of 0.1 MPa using an Amber99sb-ildn force field. Water molecules modeled with TIP3P were used as the solvent, and Na + ions were added to neutralize the charge of the system [31, 32].

The system first underwent energy minimization using the steepest descent method, followed by 100,000 steps of NVT (constant volume) and NPT (constant pressure) equilibration, with a coupling constant of 0.1 ps and a duration of 100 ps. A free molecular dynamics simulation was then carried out for 5,000,000 steps with a 2 fs time step, totaling 100 ns. After the simulation, Gromacs tools were used to analyze the trajectory and calculate the root mean square deviation (RMSD) and root mean square fluctuation (RMSF) of amino acid motions.

Statistical analyses

Data analyses and graph generation were performed using GraphPad Prism 9.0 and ImageJ. Results are presented as the mean ± standard deviation (SD) from at least three independent experiments. Differences between two groups were analyzed using an independent sample t-test. For multiple group comparisons, one-way ANOVA followed by Tukey's *post-hoc* test and repeated-measures analyses were performed. A P-value < 0.05 was considered statistically significant, with $^{*}P < 0.05$, $^{**}P < 0.01$, $^{***}P < 0.001$, and $^{****}P < 0.0001$.

Results

Conditioned medium from OGD/R-treated macrophages induces ferroptosis in cerebral endothelial cells

The establishment of the transient middle cerebral artery occlusion (tMCAO) model was confirmed by laser speckle contrast imaging and TTC staining (Fig. 1A). To assess the integrity of the blood–brain barrier (BBB) at different times after tMCAO, mouse brain tissue from the peri-infarct region was collected at 6, 12, and 24 h after tMCAO. Western blot analysis revealed a progressive disruption of BBB integrity with increasing reperfusion time, with BBB-related proteins ZO-1, occludin, and claudin-5 significantly downregulated at 24 h post-reperfusion compared to the control group (Fig. 1B). Evans blue staining and brain water content measurements demonstrated a significant increase in BBB permeability and brain edema 24 h post-tMCAO (Fig. 1C, D). Additionally, there was a notable increase in $F4/80^{+}$ cells in the brain tissue of tMCAO mice compared to the Sham group, with these cells observed in close proximity to $CD31^{+}$ cells (Fig. 1E). These findings suggest that macrophage infiltration increases following cerebral ischemia–reperfusion injury and that these infiltrating macrophages are spatially adjacent to endothelial cells.

The THP-1 cells were differentiated into macrophages and subjected to OGD/R to mimic AIS-associated macrophages (AMϕ), followed by collecting their conditioned medium (CM) for co-culture with human brain microvascular endothelial cells (HBMECs) (Fig. 1F). After OGD/R treatment, macrophages exhibited

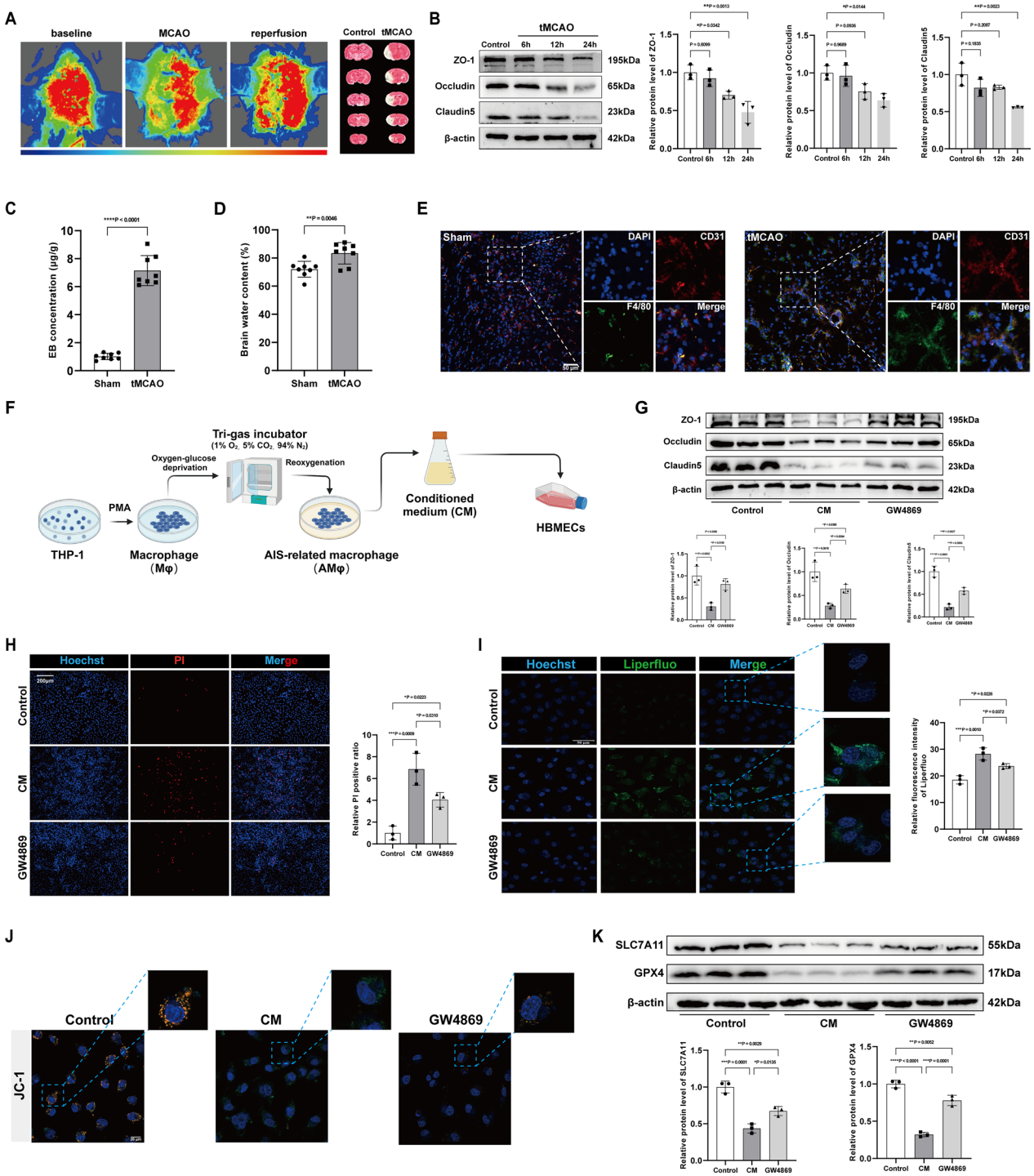

Fig. 1 Conditioned medium from OGD/R-treated macrophages induces ferroptosis in cerebral endothelial cells. **A** Laser speckle contrast imaging of cerebral blood flow and TTC staining images after tMCAO operation. **B** Representative immunoblotting and quantification of barrier-associated proteins (ZO-1, Occludin, and Claudin5) in mice brains either untreated or subjected to tMCAO surgery for 6, 12, and 24 h (n = 3). **C** Relative content of Evans blue in mouse brains (n = 8). **D** The brain water content of mice (n = 8). **E** Representative immunofluorescence images of DAPI/CD31/F4/80 staining in mouse brains. Scale bar = 50 μm. **F** Schematic diagram illustrating the co-culture of septic macrophage-conditioned medium (CM) with human brain microvascular endothelial cells (HBMECs). **G** Representative immunoblotting and quantification of barrier-associated proteins in HBMECs co-cultured with CM, with or without GW4869 treatment (n = 3). **H** Representative images and quantification of PI staining in HBMECs (n = 3). Scale bar = 200 μm. **I** Representative images and quantification of liperfluo staining in HBMECs (n = 3). Scale bar = 50 μm. **J** Representative images for mitochondrial membrane potential of HBMECs (n = 3). Scale bar = 20 μm. **K** Representative immunoblotting and quantification of SLC7A11 and GPX4 in HBMECs (n = 3). Data are presented as mean ± SD. **P* < 0.05, ***P* < 0.01, ****P* < 0.001, and *****P* < 0.0001

significant morphological changes, transitioning from round to spindle shape with increased projections (Additional file 1: Fig. S1A). Moreover, compared to the control group, OGD/R-treated macrophages showed a significant increase in mRNA levels of inflammatory factors IL-6 and TNF-α, indicating an enhanced inflammatory response (Additional file 1: Fig. S1B, C). Barrier-related protein levels were reduced in HBMECs treated with CM compared with those in the control group (Fig. 1G). CM treatment also increased the proportion of PI-positive cells, elevated lipid peroxidation levels (Fig. 1H, I), and significantly reduced mitochondrial membrane potential (Fig. 1J). Additionally, the ferroptosis markers SLC7A11 and GPX4 were markedly downregulated in the CM group compared to the control group (Fig. 1K). Pretreatment of AMϕ with the exosome synthesis/secretion inhibitor GW4869 significantly reversed these changes in HBMECs. These findings suggest that the mechanism by which AMϕ mediates ferroptosis and barrier disruption in HBMECs may be related to exosome secretion.

AMϕ-derived exosomes induce ferroptosis in brain microvascular endothelial cells

To investigate the effects of AMϕ-derived exosomes on HBMECs, exosomes were isolated from the culture medium of Mϕ and AMϕ via ultracentrifugation (Additional file 1: Fig. S2A). Both Mϕ-exo and AMϕ-exo exhibited the characteristic biconcave bilayer membrane structure typical of exosomes (Fig. 2A), with an average diameter of approximately 140 nm (Fig. 2B). They expressed exosomal markers TSG101, CD81, and CD63, with no calnexin detected (Fig. 2C). Immunofluorescence staining confirmed that PKH67-labeled exosomes were internalized by HBMECs during the co-culture (Fig. 2D). Co-culture with AMϕ-exo significantly decreased HBMEC survival over time, as shown by CCK8 assays (Fig. 2E). Flow cytometry analysis revealed a significantly higher cell death rate in the AMϕ-exo group compared to the Mϕ-exo group. However, pretreatment of HBMECs with the ferroptosis inhibitor ferrostatin-1 (Fer-1) effectively mitigated cell death (Fig. 2F). Furthermore, AMϕ-exo substantially downregulated barrier-related proteins and mitochondrial membrane potential levels in HBMECs while elevating lipid peroxidation levels (Fig. 2G–L). In addition, ferroptosis-related protein levels in HBMECs were significantly lower in the AMϕ-exo group compared to the Mϕ-exo group (Fig. 2M, N). Fer-1 treatment partially reversed these changes (Fig. 2F–N).

Exosomes derived from OGD/R-treated RAW264.7 cells mediate ferroptosis in mouse brains

To investigate the in vivo effects of AIS-related macrophage-derived exosomes, RAW264.7 cells were subjected to OGD/R treatment, and exosomes (exo) were subsequently isolated (Fig. 3A). DiR-labeled exosomes were administered to mice via tail vein injection, and ex vivo imaging confirmed the distribution of these exogenous exosomes in the brain (Fig. 3B). Colocalization of PKH67-labeled exosomes with $CD31^+$ cells in brain sections further indicated that endothelial cells internalized the exosomes (Fig. 3C). ELISA results revealed significantly elevated levels of the inflammatory cytokines IL-6 and TNF-α in the cortical tissue of the Sham + exo, tMCAO, and tMCAO + exo groups compared to the Sham group. Moreover, the tMCAO + exo group displayed higher IL-6 and TNF-α levels than the tMCAO group (Fig. 3D). Additionally, barrier disruption was more severe in the tMCAO + exo group than the tMCAO group (Fig. 3E). An increased number of Tunel-positive cells, elevated superoxide anion fluorescence, and higher levels of oxidative stress markers (GSSG, GSH, and MDA) were observed in the Sham + exo, tMCAO, and tMCAO + exo groups compared to the Sham group, with the most pronounced changes observed in the tMCAO + exo group (Fig. 3F–H). TEM analysis demonstrated mitochondrial cristae shrinkage and increased mitochondrial membrane density in the tMCAO- and exo-treated groups (Fig. 3I). Furthermore, the levels of GPX4 and SLC7A11 were significantly downregulated in the brains of the Sham + exo, tMCAO, and tMCAO + exo groups compared with those in the Sham group (Fig. 3J). These findings suggest that AIS-associated macrophage-derived exosomes induce ferroptosis in the mouse brain and exacerbate brain injury.

Identification of potential regulators in AMϕ-exo that mediate brain injury in mice

To explore key proteins involved in AMϕ-exosome (AMϕ-exo)-mediated endothelial and brain injury, we conducted proteomics sequencing of AMϕ-exo (Fig. 4A). To identify regulatory molecules in cerebral ischemia–reperfusion injury (CIRI), we analyzed AIS-related datasets (GSE30655, GSE28731, and GSE32529) from the GEO database and performed differential expression analysis (Fig. 4B, C). By intersecting these datasets, 52 differentially expressed genes (DEGs) related to AIS were identified (Fig. 4D). A PPI network of these 52 DEGs was constructed using the STRING database to identify central molecules, with an emphasis on those with high connectivity (Fig. 4E). Literature searches on central molecules present in AMϕ-exo revealed that THBS1 is closely associated with endothelial dysfunction, inflammation regulation, and oxidative stress, all of which are critical mechanisms in AIS pathology [33]. Additionally, THBS1 upregulation has been observed in ischemia–reperfusion injury models

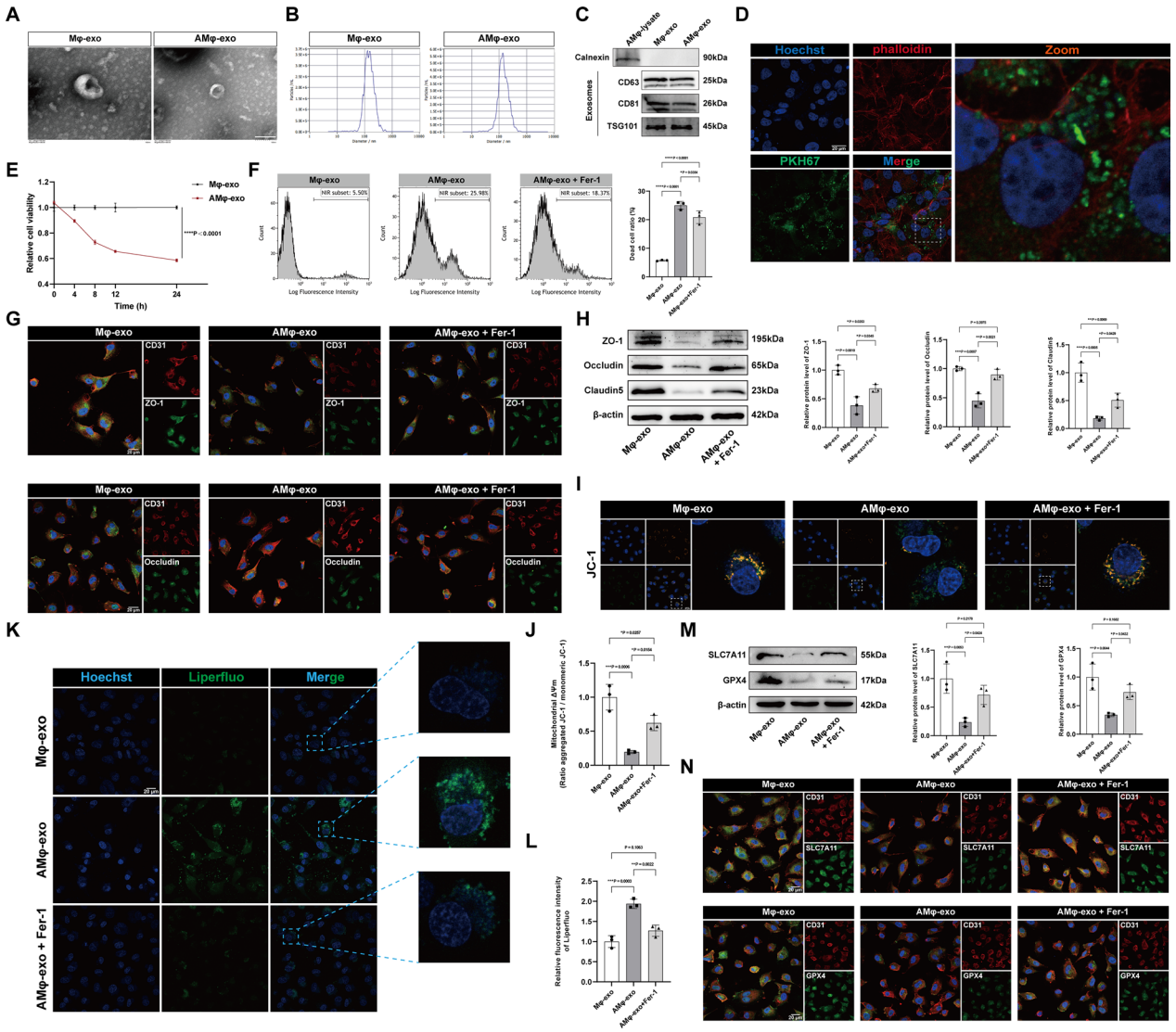

Fig. 2 AMφ-derived exosomes induce ferroptosis in brain microvascular endothelial cells. **A** Transmission electron microscopy images of exosomes isolated from the medium of Mφ and AMφ. Scale bar = 100 nm. **B** Representative nanoparticle tracking analysis images showing the distribution and average diameter of exosomes. **C** Representative immunoblotting of exosome markers. **D** Representative immunofluorescence staining of Hoechst/phalloidin/PKH67 after co-culture with human brain microvascular endothelial cells (HBMECs) using PKH67-labeled exosomes. Scale bar = 20 μm. **E** Quantification of CCK8 assays performed on HBMECs co-cultured with Mφ-exo and AMφ-exo (n = 5). **F** Representative images and quantification of the Zombie NIR™ staining in HBMECs co-cultured with Mφ-exo and AMφ-exo in the presence or absence of ferrostatin-1 (Fer-1) (n = 3). **G** Representative immunofluorescence staining for DAPI/CD31/ZO-1 and DAPI/CD31/Occludin in HBMECs. Scale bar = 20 μm. **H** Representative immunoblotting and quantification of barrier-associated proteins (ZO-1, Occludin and Claudin5) in HBMECs (n = 3). **I**, **J** Representative images and quantification of mitochondrial membrane potential of HBMECs (n = 3). Scale bar = 20 μm. **K**, **L** Representative images of liperfluo staining and quantitative analysis of liperfluo fluorescence intensity in HBMECs (n = 3). Scale bar = 20 μm. **M** Representative immunoblotting and quantification of SLC7A11 and GPX4 in HBMECs (n = 3). **N** Representative images of immunofluorescence staining for DAPI/CD31/SLC7A11 and DAPI/CD31/GPX4 in HBMECs. Scale bar = 20 μm. Data are presented as mean ± SD. *$P < 0.05$, **$P < 0.01$, ***$P < 0.001$, and ****$P < 0.0001$

[34]. To investigate THBS1 expression in ischemic stroke and its association with macrophages, we analyzed single-cell RNA sequencing (scRNA-seq) data from middle cerebral artery occlusion (MCAO) mouse brain tissue. The results revealed a higher proportion of THBS1-expressing macrophages in the MCAO group compared to the Sham group (Fig. 4F, G). Pseudotime analysis indicated that macrophages with low THBS1 expression were located at the initial differentiation state (Fig. 4H).

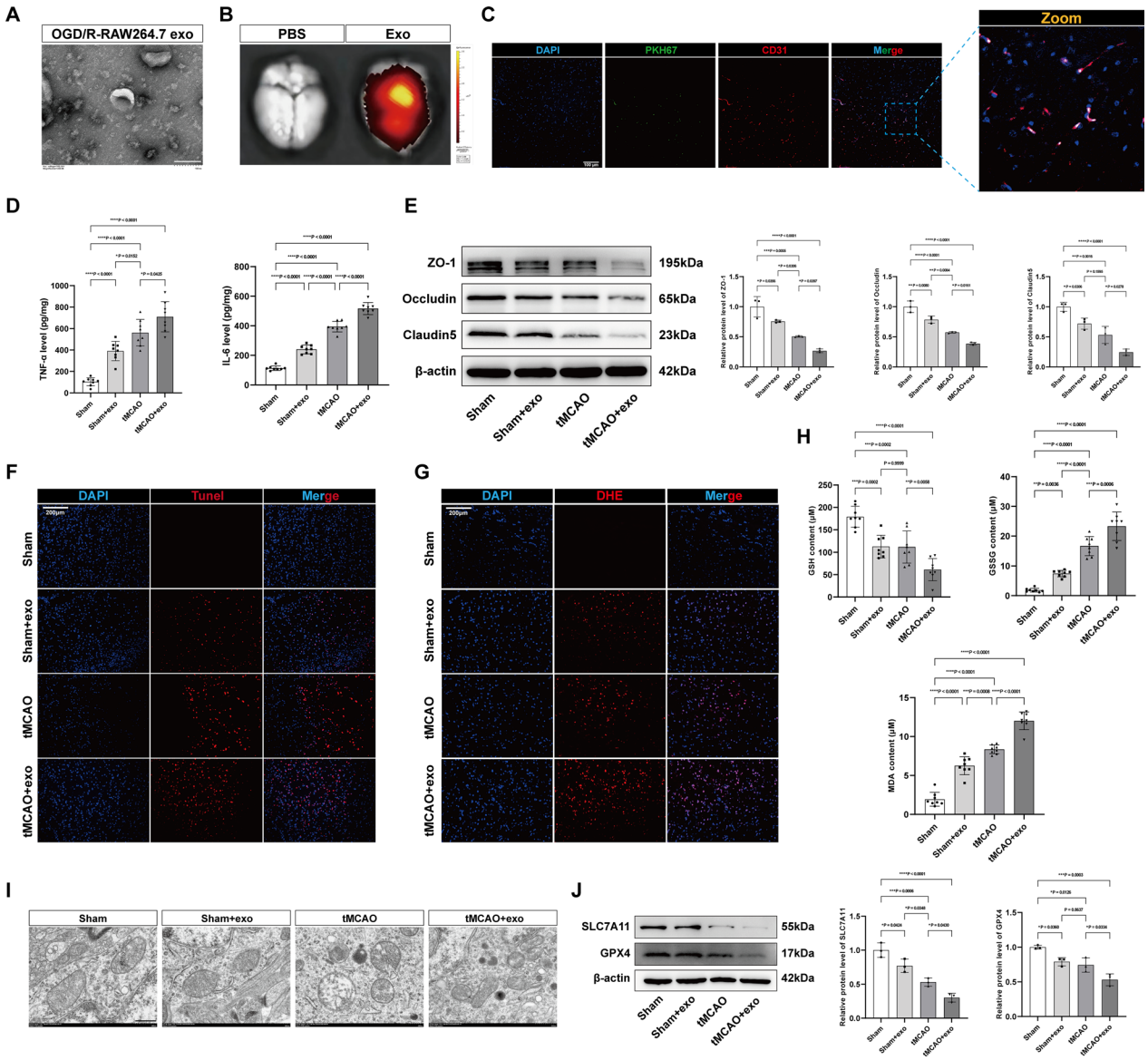

Fig. 3 Exosomes derived from OGD/R-treated RAW264.7 cells mediate ferroptosis in mouse brains. **A** Transmission electron microscopy (TEM) images of the isolated exosomes from the OGD/R-treated RAW264.7 cells. Scale bar = 100 nm. **B** In vivo fluorescence images of brains in mice with or without DiR-labeled exosomes. **C** Representative immunofluorescence staining for DAPI/CD31/PKH67 in mouse brains after tail vein injection of PKM67-labeled exosomes. Scale bar = 100 μm. **D** Quantification of TNF-α, and IL-6 levels in mouse brains (n = 8). **E** Representative immunoblotting and quantification of barrier-associated proteins (ZO-1, Occludin, and Claudin5) in mouse brains (n = 3). **F** Representative images of Tunel staining of mouse brains and quantification of Tunel-positive cells (n = 3). Scale bar = 200 μm. **G** Representative images of DHE staining of mouse brains and quantification of DHE fluorescence intensity (n = 3). Scale bar = 200 μm. **H** Quantification of GSSG, GSH, and MDA levels in mouse brains (n = 8). **I** TEM image of mouse brains. Scale bar = 500 nm. **J** Representative immunoblotting and quantification of SLC7A11 and GPX4 in mouse brains (n = 3). Data are presented as mean ± SD. *$P < 0.05$, **$P < 0.01$, ***$P < 0.001$, and ****$P < 0.0001$

Furthermore, THBS1 was significantly upregulated in plasma exosomes from AIS patients and was positively correlated with blood–brain barrier (BBB) damage markers MMP-9 and S100B (Fig. 4I–M). Clinical samples and in vivo and in vitro experiments provided further validation. THBS1 expression was elevated in OGD/R-treated THP-1 and RAW264.7 macrophages and their secreted exosomes (Fig. 4N, S3A–D). Similar upregulation of THBS1 was observed in peripheral blood monocytes from AIS patients and in the brains of tMCAO mice (Fig. 4N. HBMECs co-cultured with AMφ-exo exhibited higher THBS1 levels than those co-cultured with

Mφ-exo (Fig. 4O). THBS1 was also highly expressed in macrophages isolated from the brains of tMCAO mice (Fig. 4P). Based on these multi-level analyses, we propose THBS1 as a key regulatory molecule in macrophage-derived exosome-mediated brain injury during CIRI, warranting further investigation and functional validation.

THBS1 in macrophage-derived exosomes mediates endothelial cell ferroptosis and barrier disruption during CIRI

In this study, three RNA interference sequences were used to silence THBS1 in macrophages, and the most efficient sequence was selected for subsequent experiments (Fig. 5A). Exosomes were isolated from AMφ transfected with siTHBS1 (siTHBS1-AMφ-exo) and co-cultured with HBMECs (Fig. 5B). The results indicated that THBS1 silencing reversed AMφ-exo-induced cell death and oxidative stress (Fig. 5C, D). Compared to the Mφ-exo group, the siNC-AMφ-exo group exhibited decreased expressions of barrier- and ferroptosis-related proteins, reduced mitochondrial membrane potential, and increased lipid peroxidation levels (Fig. 5E, F). These changes were attenuated by THBS1 silencing (Fig. 5E, F). Furthermore, we constructed a plasmid to overexpress THBS1 and transfected it into THP-1 cells, which significantly increased THBS1 protein and mRNA levels (Fig. 5G). As expected, THBS1 overexpression markedly elevated ROS levels in HBMECs co-cultured with AMφ-exo while decreasing the levels of barrier- and ferroptosis-related proteins (Fig. 5H, I).

To validate the in vivo effects, exosomes from OGD/R-treated RAW264.7, transfected with either siThbs1 or oeThbs1 (siThbs1-exo or oeThbs1-exo), were injected into mice via the tail vein (Additional file 1: Fig. S4A-D). Evans blue staining revealed that compared to the tMCAO + siNC-exo group, BBB permeability was significantly reduced in the tMCAO + siThbs1-exo group (Additional file 1: Fig. S4E). Tunel and DHE staining further indicated that Thbs1 silencing mitigated the exosome-induced increases in cell death and superoxide anion levels in the mouse brain (Additional File 1: Fig. S4F, G). Additionally, compared with the tMCAO + siNC-exo group, barrier- and ferroptosis-related proteins were significantly upregulated in the tMCAO + siThbs1-exo group, whereas Thbs1 overexpression exacerbated the loss of both barrier and protective ferroptosis-related proteins (Additional file 1: Fig. S4H, I).

Thbs1 knockdown in macrophages inhibits BBB disruption and alleviates brain injury

To evaluate the in vivo effects of Thbs1 knockdown in macrophages, a macrophage-specific adeno-associated virus was used for Thbs1 (Fig. 6A). This approach significantly decreased Thbs1 levels in the mouse brain without altering normal brain structure (Fig. 6B, Additional file 1: Fig. S5A, B). The results showed that macrophage-specific Thbs1 knockdown significantly improved BBB permeability while reducing neuroinflammation and oxidative stress (Fig. 6C–F). Furthermore, the proportion of $CD31^{+}/GPX4^{+}$ cells in the peri-infarct brain tissue was markedly higher in the tMCAO + AAV-shThbs1 group than that in the tMCAO and tMCAO + AAV-shNC groups (Fig. 6G). These findings indicated that Thbs1 knockdown in macrophages effectively alleviated BBB disruption and brain injury.

Macrophage-derived THBS1 contributes to CIRI by inhibiting GPX4 in endothelial cells

Endothelial cell-specific Gpx4 knockout (Gpx4cko) mice were generated using the Cre-LoxP system (Fig. 7A, B). After inducing tMCAO in both $Gpx4^{f/f}$ and $Gpx4^{cko}$ mice, we observed that Gpx4 knockout led to significantly increased BBB permeability and a more pronounced reduction in barrier proteins. Treatment with AAV-shThbs1 in $Gpx4^{f/f}$ mice partially alleviated the increased BBB permeability and brain injury; however, no significant improvement was observed in $Gpx4^{cko}$

(See figure on next page.)

Fig. 4 Identification of potential regulators in AMφ-exo that mediate brain injury in mice. **A** Heatmap of AMφ-exo proteomics sequencing. **B**, **C** Heatmaps (**B**) and volcano plots (**C**) of genes in the GSE30655, GSE28731, and GSE32529 datasets. **D** Venn diagram of differentially expressed genes (DEGs) for the GSE30655, GSE28731, and GSE32529 datasets. **E** Protein–protein interaction network diagram. **F** UMAP plot of cells clustered according to the expression of known marker genes and scatter plot showing THBS1 expression in eight cell types. **G** Proportional graph displaying the proportion of high and low THBS1 expression in macrophages of tMCAO mice and Sham mice. **H** Cell trajectories displayed according to pseudotime, which are chronologically ordered based on dark-to-light color indications, and expression distribution of THBS1 in the pseudotime analysis. **I–K** Levels of THBS1 (**I**) in exosomes from plasma of healthy volunteers (n = 32) and patients with AIS (n = 56), as well as levels of MMP-9 (**J**) and S100B (**K**) in plasma. **L**, **M** Correlation of THBS1 levels in exosomes with levels of MMP-9 (**L**) and S100B (**M**) in plasma. **N** Representative immunoblotting and quantification of THBS1 in THP-1 and RAW264.7 cells and exosomes secreted by both, in peripheral blood monocytes from clinical samples, and in mouse brains. **O** Representative images of immunofluorescence staining for DAPI/THBS1 in HBMECs treated with Mφ-exo and AMφ-exo. Scale bar = 20 μm. **P** Representative images of immunofluorescence staining for DAPI/F4/80/THBS1 in the brains of mice with or without tMCAO operation. Scale bar = 100 μm. Data are presented as mean ± SD. $^{*}P < 0.05$, $^{**}P < 0.01$, $^{***}P < 0.001$, and $^{****}P < 0.0001$

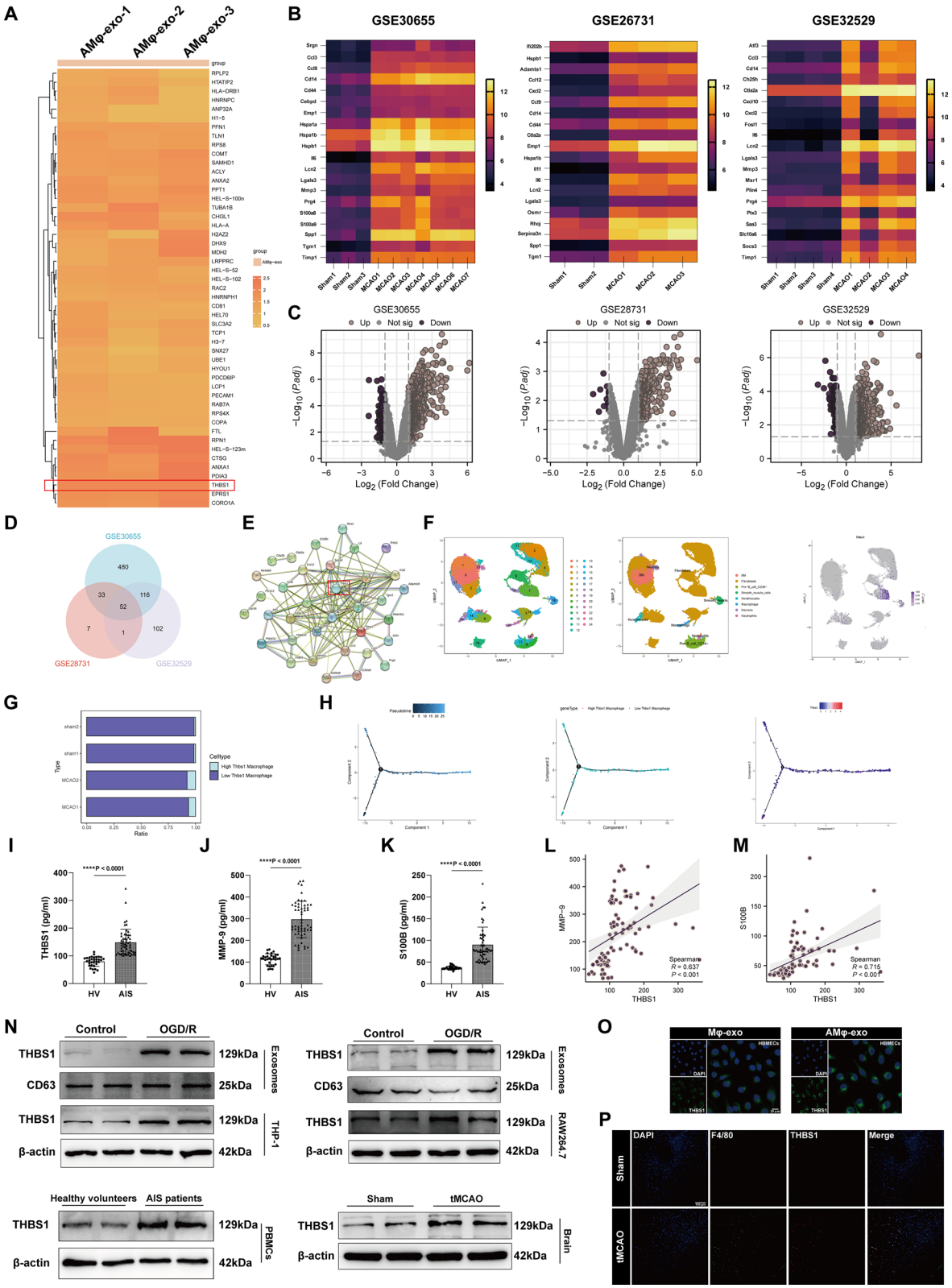

Fig. 4 (See legend on previous page.)

mice treated with AAV-shThbs1 (Fig. 7C–H). These findings suggest that macrophage-derived THBS1-mediated endothelial barrier disruption is linked to GPX4 inhibition in endothelial cells.

THBS1 promotes GPX4 ubiquitination and degradation through interaction with OTUD5

To further investigate the specific regulatory mechanism of THBS1 in AMϕ-exo on GPX4 in endothelial cells, we examined the ubiquitination levels of GPX4 in HBMECs co-cultured with AMϕ-exo. The results showed a significant increase in GPX4 ubiquitination in HBMECs following AMϕ-exo treatment, which was alleviated by THBS1 knockdown (Fig. 8A). Additionally, pretreatment of HBMECs with the proteasome inhibitor, MG132, blocked GPX4 degradation, indicating that the reduction in GPX4 was mediated by the proteasome pathway (Fig. 8B). Furthermore, treatment of HBMECs with the protein synthesis inhibitor cycloheximide (CHX) demonstrated that AMϕ-exo-induced GPX4 reduction was independent of new protein synthesis (Fig. 8C). However, the co-immunoprecipitation results showed no direct interaction between THBS1 and GPX4 (Additional file 1: Fig. S6A, B), suggesting that THBS1 regulates GPX4 ubiquitination through an intermediate molecule. Previous studies identified OTUD5 as a key deubiquitinase involved in regulating GPX4 ubiquitination [35]. Therefore, we explored whether OTUD5 mediates the regulatory effect of THBS1 on GPX4 expression. Protein–protein docking analysis suggested a potent binding potential between THBS1 and OTUD5 (Fig. 8D), which was confirmed by co-immunoprecipitation (Fig. 8E). Immunofluorescence staining further revealed the co-localization of THBS1 and OTUD5 in AMϕ-exo-treated HBMECs (Fig. 8F). Silencing OTUD5 increased GPX4 ubiquitination in HBMECs co-cultured with siTHBS1-AMϕ-exo (Fig. 8G). These findings indicated that in CIRI, THBS1 in macrophage-derived exosomes modulates OTUD5 deubiquitinase activity, thereby affecting GPX4 levels in endothelial cells.

Salvianolic acid B inhibits GPX4 ubiquitination by disrupting the interaction between THBS1 and OTUD5

The above studies indicate that THBS1 plays a critical role in macrophage-mediated ferroptosis of brain microvascular endothelial cells during CIRI. To enhance the translational potential of this research, we aim to identify compounds that can modulate THBS1. In recent years, natural small molecules have emerged as a valuable resource in drug development due to their structural diversity and biological activity. Therefore, we targeted THBS1 and employed a natural small molecule compound library combined with high-throughput screening to identify molecules capable of regulating THBS1 (Fig. 9A, Additional file 1: Table S4). We focused on screening small molecules with strong binding affinity for THBS1, identifying salvianolic acid B (SAB) as the second-highest binder, with a binding energy of -62.21 kcal/mol (Fig. 9B, C). However, its effect on CIRI remains unexplored. Therefore, we conducted further investigations into the role of SAB. Molecular dynamics simulations were performed to assess the stability of this interaction. The RMSD results indicated that the SAB-THBS1 complex reached a stable state after 5 ns (Fig. 9D). Additionally, the low RMSF values near the 190th amino acid residue suggested that this region was a potential binding site (Fig. 9E). CETSA results demonstrated that SAB treatment increased the resistance of THBS1 cells to degradation, supporting the hypothesis of their interaction (Fig. 9F, G). Interestingly, SAB did not alter the levels of THBS1 or OTUD5 in HBMECs but did inhibit their interaction (Fig. 9H). Furthermore, SAB partially suppressed AMϕ-exo-induced GPX4 ubiquitination (Fig. 9I). These findings suggest that SAB inhibits GPX4 ubiquitination by interfering with the interaction between THBS1 and OTUD5.

(See figure on next page.)

Fig. 5 THBS1 in macrophage-derived exosomes mediates endothelial cell ferroptosis and barrier disruption during CIRI. **A** Representative immunoblotting was conducted to validate the efficiency of THBS1 silencing in THP-1 cells and AMϕ-exo, along with RT-qPCR analysis to assess THBS1 mRNA expression in THP-1 cells (n = 4). **B** Transmission electron microscopy images of the isolated exosomes of AMϕ after silencing THBS1. Scale bar = 100 nm. **C** Representative images and quantification of the Zombie NIR™ staining in HBMECs co-cultured with Mϕ-exo and AMϕ-exo with or without silencing THBS1 (n = 3). **D** Quantification of GSSG, GSH, and MDA in HBMECs (n = 8). **E** Representative immunoblotting and quantification of barrier-associated proteins (ZO-1, Occludin and Claudin5) and ferroptosis-associated proteins (SLC7A11 and GPX4) in HBMECs (n = 3). **F** Representative images and quantification for liperfluo staining and mitochondrial membrane potential of HBMECs (n = 3). Scale bar = 20 μm. **G** Representative immunoblotting for efficiency validation after overexpressing THBS1 and RT-qPCR analysis to determine mRNA expression of THBS1 in THP-1 cells (n = 4). **H** Representative images and quantification of the ROS staining in HBMECs co-cultured with Mϕ-exo and AMϕ-exo with or without overexpressing THBS1 (n = 3). Scale bar = 200 μm. **I** Representative immunoblotting and quantification of barrier-associated proteins (ZO-1, Occludin and Claudin5) and ferroptosis-associated proteins (SLC7A11 and GPX4) in HBMECs (n = 3). Data are presented as mean ± SD. *$P < 0.05$, **$P < 0.01$, ***$P < 0.001$, and ****$P < 0.0001$

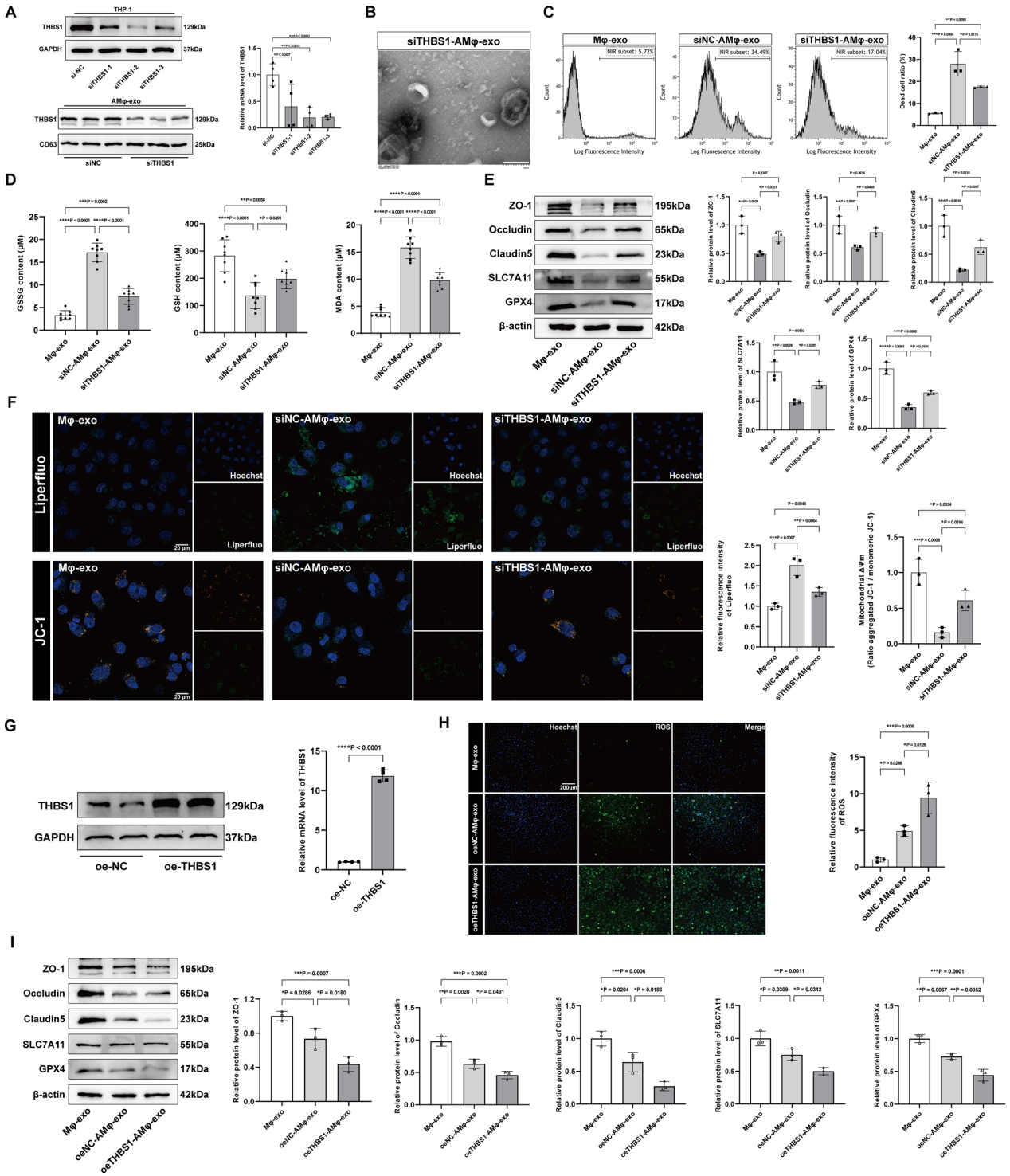

Fig. 5 (See legend on previous page.)

THBS1 inhibition combined with SAB treatment improves BBB integrity and neurological deficits in tMCAO mice

To assess the sensorimotor function in tMCAO mice, neurological behavioral tests, including adhesive removal and corner tests, were conducted over a 14-day period. Both THBS1 inhibition and SAB treatment significantly reduced the time to contact and

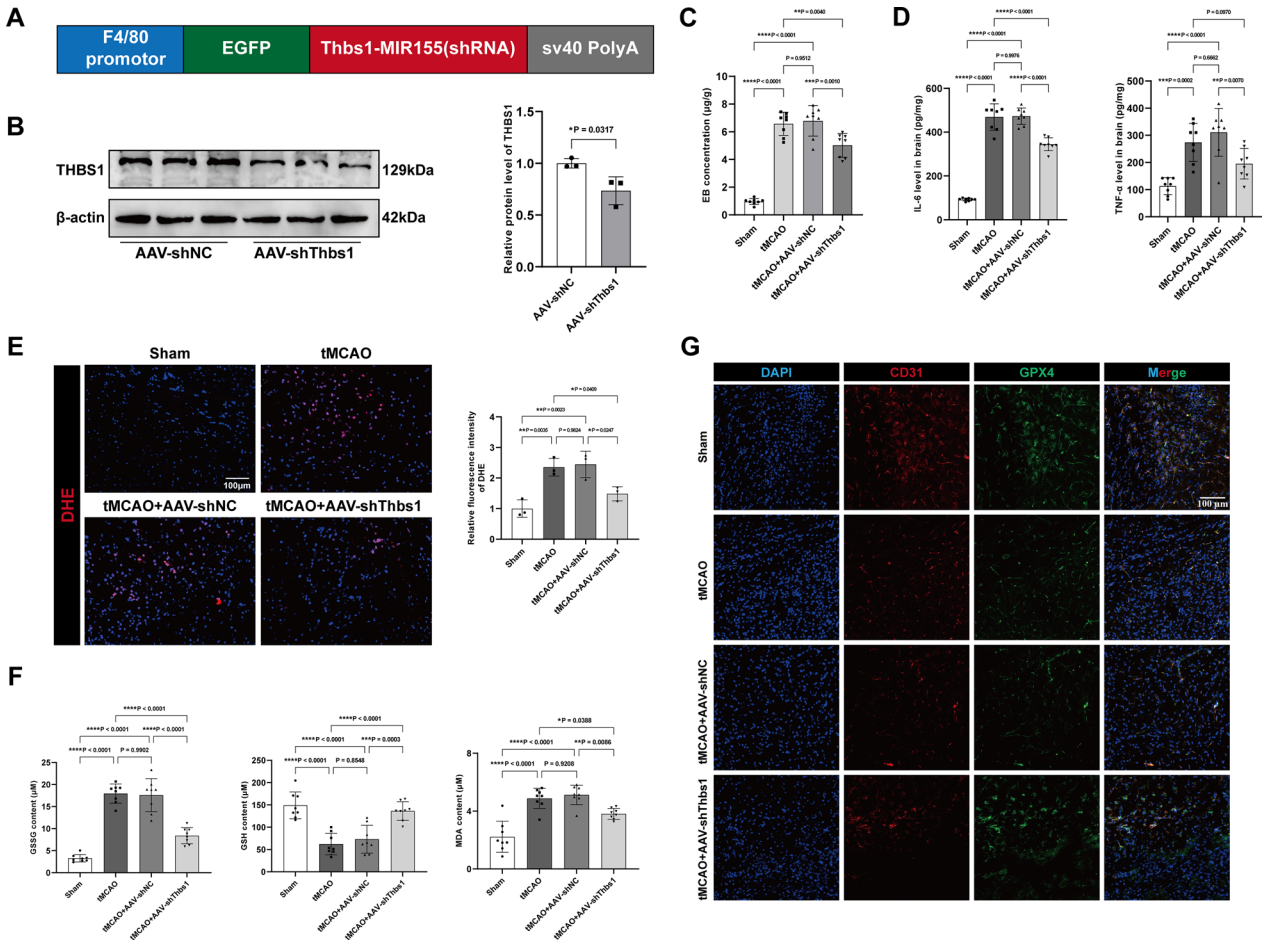

Fig. 6 Thbs1 knockdown in macrophages inhibits BBB disruption and alleviates brain injury. **A** Schematic representation of AAV vector construction targeting the knockdown of THBS1 in macrophages. **B** Representative images and quantification of immunoblotting of THBS1 in mouse brains after tail vein injection of AAV-shNC and AAV-shThbs1 (n = 3). **C** Relative content of Evans blue in mouse brains (n = 8). **D** Quantification of IL-6 and TNF-α in mouse brains (n = 8). **E** Representative images of DHE staining of mouse brains and quantification of DHE fluorescence intensity (n = 3). Scale bar = 100 μm. **F** Quantification of GSSG, GSH, and MDA in mouse brains (n = 8). **G** Representative images of immunofluorescence staining for DAPI/CD31/GPX4 in mouse brains. Scale bar = 100 μm. Data are presented as mean ± SD. *$P < 0.05$, **$P < 0.01$, ***$P < 0.001$, and ****$P < 0.0001$

removal in the adhesive removal test, as well as the left turn rate in the corner test. These effects were most pronounced in the group that received the combination of THBS1 inhibition and SAB treatment (Fig. 10A, B). Nissl staining further demonstrated that the intensity of Nissl bodies in the cerebral cortical tissue of the ischemic penumbra region increased after treatment, and the largest increase was observed in the combination treatment group (Fig. 10C). These findings indicate that the combination of THBS1 inhibition and SAB improves both sensory and motor deficits as well as neuronal damage in tMCAO mice. Furthermore, the combination treatment demonstrated superior efficacy in reducing oxidative stress levels and improving BBB permeability in brain tissue compared with either treatment alone (Fig. 10D, E).

Discussion

Currently, there is no effective clinical treatment for CIRI caused by brain ischemia and subsequent reperfusion. BBB disruption is a key factor in the various pathological mechanisms of CIRI. The BBB is a semi-permeable barrier composed of endothelial cells, tight junctions, pericytes, astrocytes, and extracellular matrix [36]. Identifying the factors that mediate damage to cerebral microvascular endothelial cells and tight junctions in CIRI is crucial for improving long-term patients with AIS [37].

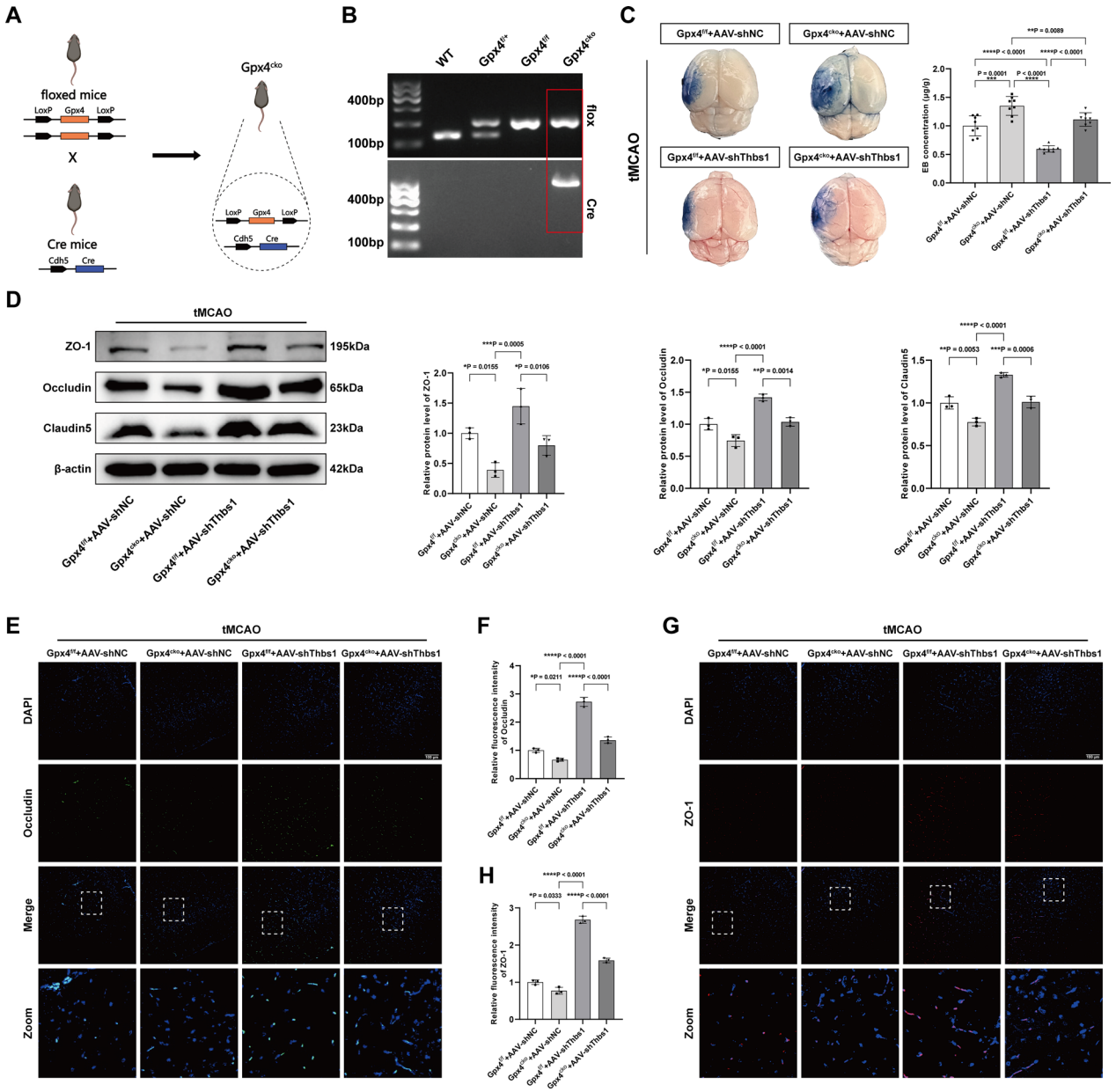

Fig. 7 Macrophage-derived THBS1 contributes to CIRI by inhibiting GPX4 in endothelial cells. **A** Schematic diagram of the construction of Gpx4^{cko} mouse. **B** Representative images for mouse genotyping. **C** Representative images and quantification of Evans blue staining of mouse brains of Gpx4$^{f/f}$ or Gpx4^{cko}, with or without AAV-shNC or AAV-shThbs1 treatment and then receiving tMCAO. **D** Representative immunoblotting and quantification of ZO-1, Occludin, and Claudin5 proteins in mouse brains (n = 3). **E–H)** Representative images and quantification of immunofluorescence staining for DAPI/CD31/Occludin **(E, F)** and DAPI/CD31/ZO-1 **(G, H)** in mouse brains. Scale bar = 100 μm. Data are presented as mean ± SD. *$P < 0.05$, **$P < 0.01$, ***$P < 0.001$, and ****$P < 0.0001$

Heightened reactivity of peripheral monocytes/macrophages and their increased infiltration into brain tissue are critical pathological features of the acute phase of acute ischemic stroke (AIS) [38, 39]. Our study found that endothelial cells and macrophages in mouse brain tissue are located in close proximity, providing a spatial basis for their interaction. Previous studies have shown that exosomes derived from pro-inflammatory macrophages mediate endothelial mitochondrial dysfunction through non-coding RNA, promote ROS production, and contribute to endothelial-mesenchymal transition, thereby exacerbating spinal cord injury [17]. Additionally, in the myocardial infarction microenvironment, M1-like macrophages increase exosome secretion,

downregulating Sirtuin 1 and AMP-activated protein kinase α2 in endothelial cells, ultimately inhibiting cell viability and angiogenesis [16]. Therefore, we propose that macrophage activity may contribute to cerebral microvascular endothelial damage and BBB disruption during CIRI. In the present study, THP-1 cells were differentiated into macrophages and subjected to OGD/R to simulate the state of macrophages during the acute phase of CIRI. OGD/R-treated macrophages exhibited loss of their original morphology, developed multiple elongated protrusions, and showed significantly increased expression of pro-inflammatory factors, indicative of M1-like differentiation. This transformation effectively mimics macrophage activation in the acute phase of CIRI [40].

Macrophages subjected to oxygen–glucose deprivation increase exosome secretion, facilitating communication with other cells, and contribute to disease progression [16]. In this study, we found that pretreatment of AMϕ with the exosome secretion inhibitor GW4869 partially alleviated CM-induced HBMEC damage, suggesting that exosomes play a critical role in this process and warrant further investigation. However, GW4869 did not completely prevent the harmful effects of AMϕ-conditioned medium on endothelial cells. This may be attributed to cytokines and other bioactive substances secreted by AMϕ, though further confirmation is needed. Ferroptosis is characterized by lipid peroxidation and abnormal iron metabolism. It involves a dynamic balance between the oxidative system, composed of iron ions, the Fenton reaction, and ROS, and the antioxidant system, consisting of GPX4, glutathione (GSH), the glutamate transport system, and other newly discovered pathways that maintain cellular and systemic homeostasis [41]. Ischemia and reperfusion disrupt the balance between oxidative and antioxidant systems and iron homeostasis in the brain, leading to widespread ferroptosis during CIRI [42]. In this study, we observed that HBMECs co-cultured with AMϕ-exo exhibited significantly decreased levels of GSH, SLC7A11, and GPX4, alongside increased levels of GSSG, MDA, lipid peroxides, and ROS, suggesting that AMϕ-exo disrupts the oxidative balance in endothelial cells. The administration of the ferroptosis inhibitor Fer-1 reversed these changes, indicating that AMϕ-exo-mediated endothelial cell damage is associated with ferroptosis.

To evaluate the in vivo effects of macrophage-derived exosomes under stroke conditions while maintaining species consistency, RAW264.7 cells were subjected to OGD/R treatment, and their enriched exosomes (exo) were injected into mice. The results showed that exosomes secreted by macrophages in the CIRI state induced ferroptosis and disrupted BBB function in both Sham and tMCAO mice, exacerbating brain injury. Furthermore, we labeled exosomes with PKH67 and examined their endothelial uptake after tail vein injection. These results indicated that CD31-positive endothelial cells in the mouse brain internalized PKH67-labeled exosomes. Because macrophage-derived exosomes regulate various cell types based on in vivo and in vitro experiments, we propose that exosome-mediated brain tissue injury is at least partially related to the direct disruption of cerebral vascular endothelial cells.

This study employed proteomic analysis of AMϕ-exo to identify key proteins involved in cerebrovascular barrier damage. Through the integration of transcriptomic data from public databases, single-cell sequencing results, and a thorough literature review, THBS1 was identified as a target protein. THBS1 is an antiangiogenic factor that is highly expressed in response to injurious stimuli [43]. THBS1 is released via exosomes, mediates intercellular communication, and regulates cellular functions [44]. Moreover, THBS1 levels in infarcted brain tissue remain elevated for up to 72 h after ischemia–reperfusion injury in mice [45]. However, the role of THBS1 in brain endothelial cells during CIRI has not been previously described. Our study revealed that THBS1 is highly expressed not only in exosomes from OGD/R-treated macrophages but also in the serum exosomes of patients with AIS, showing a positive correlation with markers of vascular barrier damage, suggesting its potential impact on BBB integrity. Further experiments confirmed that THBS1 is a critical driver of macrophage exosome-mediated ferroptosis in brain endothelial cells during CIRI, contributing to brain tissue injury. Studies

(See figure on next page.)

Fig. 8 THBS1 promotes GPX4 ubiquitination and degradation through interaction with OTUD5. **A** Representative images and quantification of immunoblotting of GPX4 protein and its ubiquitination in HBMECs co-cultured with AMϕ-exo with or without silencing THBS1 (n = 3). **B** Representative images and quantification of immunoblotting of GPX4 in HBMECs in the presence or absence of MG132 pretreatment (n = 3). **C** Representative images and quantification of immunoblotting of GPX4 in HBMECs with and without cycloheximide (CHX) pretreatment (n = 3). **D** Binding model of THBS1 and OTUD5 and the residues detail of the interaction. **E** Representative images of co-immunoprecipitations used to assess the binding between THBS1 and OUTD5. **F** Representative images and quantification of fluorescence intensity of immunofluorescence staining for DAPI/THBS1/OTUD5 in HBMECs treated with AMϕ-exo. Scale bar = 2 μm. **G** Representative images of immunoblotting of GPX4 protein and its ubiquitination levels in HBMECs co-cultured with AMϕ-exo with or without silencing THBS1 or OTUD5. Data are presented as mean ± SD. *$P < 0.05$, **$P < 0.01$, ***$P < 0.001$, and ****$P < 0.0001$

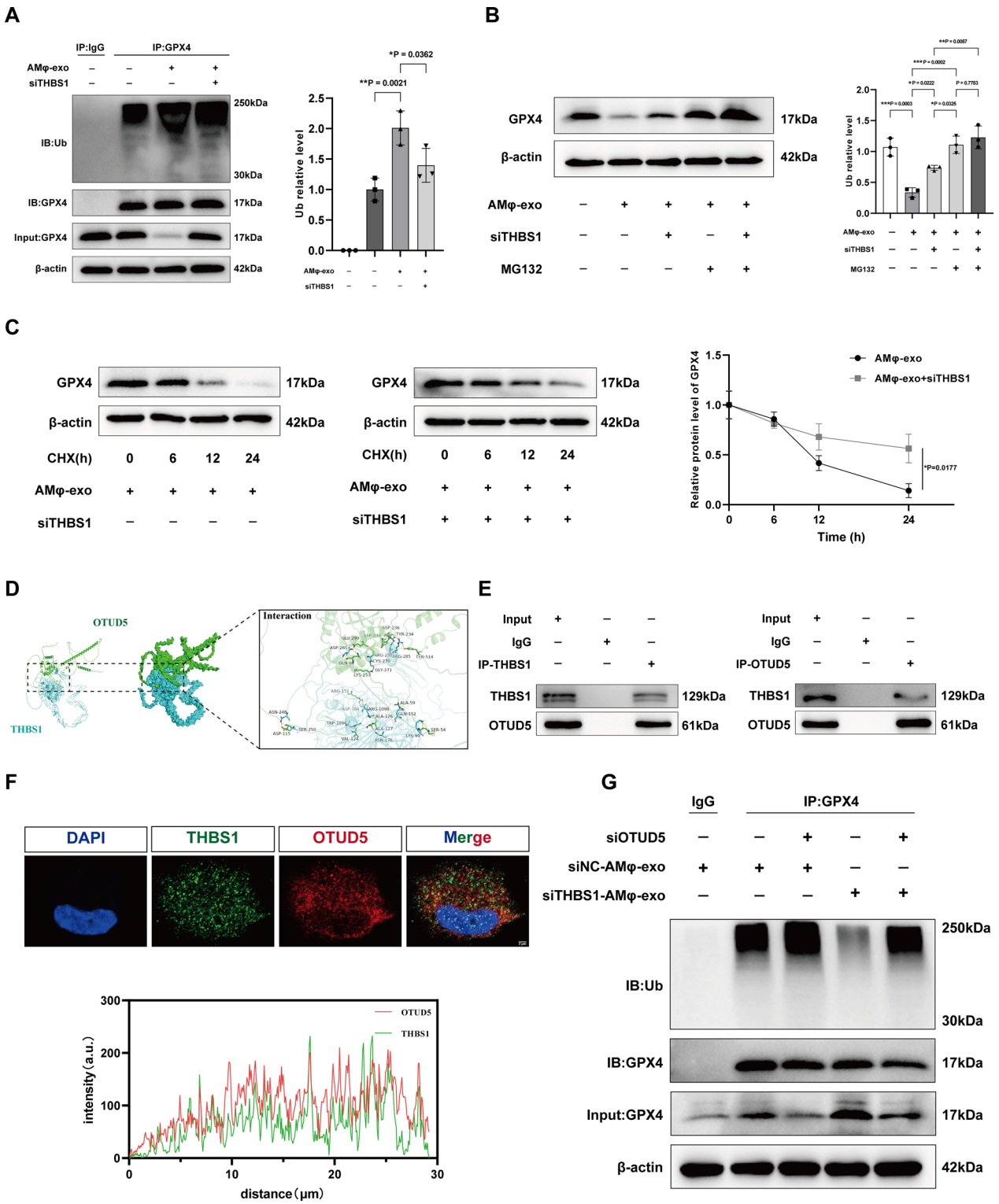

Fig. 8 (See legend on previous page.)

have shown elevated THBS1 levels in neurons promote neuronal apoptosis and endoplasmic reticulum stress in rats [33]. Conversely, THBS1 in astrocytes supports synaptic remodeling in neurons [46], suggesting that astrocytic THBS1 may facilitate neuronal repair during the subacute and chronic phases of CIRI. These findings

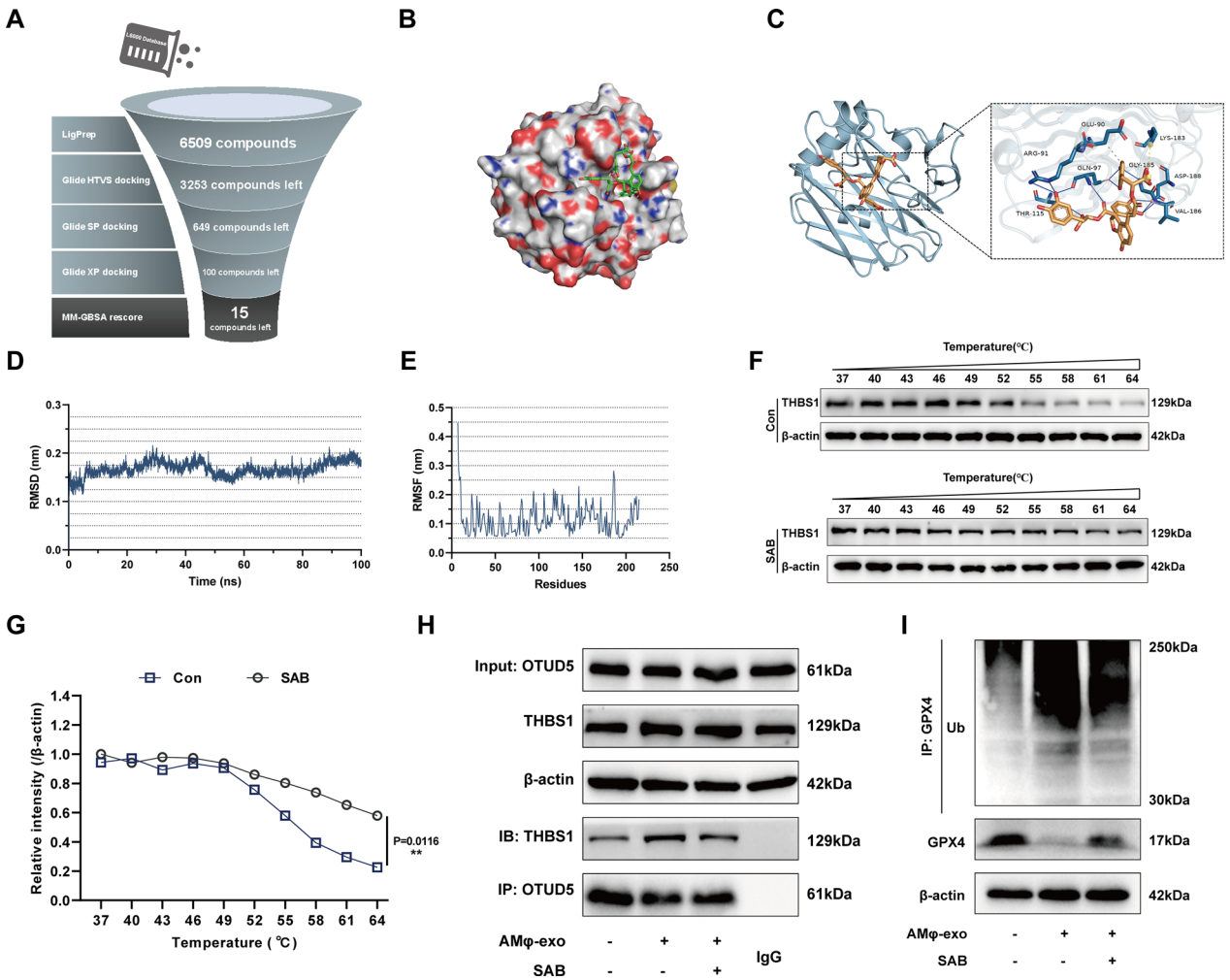

Fig. 9 Salvianolic acid B inhibits GPX4 ubiquitination by disrupting the interaction between THBS1 and OTUD5. **A** Overview of the compound screening scheme. **B**, **C** The representative docking complex of THBS1 and salvianolic acid B (SAB). **D**, **E** Root mean square deviation (RMSD) and root mean square fluctuation (RMSF) values of the THBS1-SAB docking complex. **F**, **G** Cellular thermal shift assay between SAB and THBS1 (**F**) and the quantification **(G)** (n = 3). **H** Representative immunoblot images of THBS1 and OTUD5, along with co-immunoprecipitation images assessing the binding between THBS1 and OTUD5. **I** Representative images of immunoblotting of GPX4 protein and its ubiquitination levels in HBMECs co-cultured with AMφ-exo, with or without SAB treatment. Data are presented as mean ± SD. *$P < 0.05$, **$P < 0.01$, ***$P < 0.001$, and ****$P < 0.0001$

underscore the complex role of THBS1 in brain injury, with temporal and spatial heterogeneity. Investigating the function of THBS1 in various brain cell types and its influence on brain injury could provide valuable insights for developing THBS1-targeted precision therapies for CIRI. This study is the first to demonstrate the role of macrophage-derived THBS1 in mediating endothelial dysfunction during CIRI, offering further mechanistic insights into the contribution of THBS1 to brain injury.

This study demonstrated that silencing THBS1 in macrophages reduces exosome-mediated ferroptosis in brain vascular endothelial cells, accompanied by increased SLC7A11 and GPX4 protein levels. These findings suggest that THBS1 regulates endothelial ferroptosis, potentially through multiple ferroptosis-related factors. GPX4 plays a pivotal role in ferroptosis by preventing lipid peroxide accumulation and utilizing GSH transported via SLC7A11 to eliminate lipid peroxides [47]. Furthermore, GPX4 counteracts ACSL4-mediated excessive lipid peroxidation, thereby inhibiting ferroptosis [48]. Recognizing the critical regulatory role of GPX4 in ferroptosis, this study further investigated the mechanisms underlying THBS1-mediated GPX4 downregulation in subsequent experiments. Recent studies have identified abnormal ubiquitination of GPX4 in several diseases that are closely linked to ferroptosis. Under

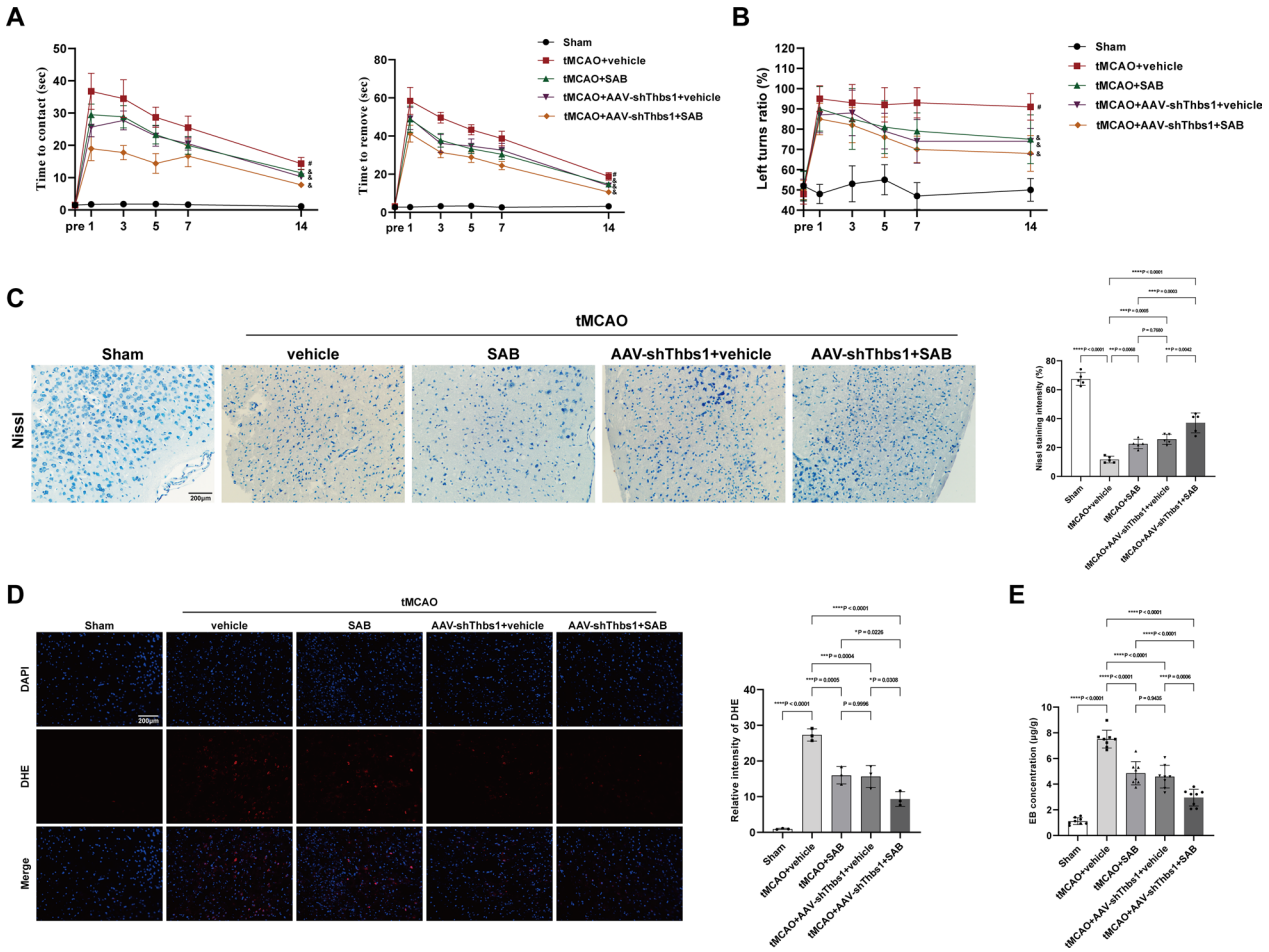

Fig. 10 THBS1 inhibition combined with SAB treatment improves BBB integrity and neurological deficits in tMCAO mice. **A** The time to contact and remove the tape in mice subjected to different treatment regimens within 14 days post-surgery in the adhesive remove test (n = 8). $^{\#}P < 0.05$ vs Sham, $^{\&}P < 0.05$ vs tMCAO. **B** The ratio of left turns in the corner test (n = 8). $^{\#}P < 0.05$ vs Sham, $^{\&}P < 0.05$ vs tMCAO. **C** Representative images and quantification of Nissl staining in the cerebral cortical tissue of the ischemic penumbra region (n = 5). Scale bar = 200 μm. **D** Representative images and quantification of DHE staining of mouse brains (n = 3). Scale bar = 200 μm. **E** Relative content of Evans blue in mouse brains (n = 8). Data are presented as mean ± SD. $^{*}P < 0.05$, $^{**}P < 0.01$, $^{***}P < 0.001$, and $^{****}P < 0.0001$

oxidative stress, GPX4 is stabilized by the formation of linear ubiquitin chains that inhibit ferroptosis [49]. Several studies have explored the potential of modulating GPX4 ubiquitination to influence disease progression, yielding promising results and highlighting the critical role of ubiquitination in maintaining GPX4 homeostasis [50, 51]. However, it remains unclear whether the downregulation of GPX4 in CIRI is associated with abnormal ubiquitination. Our study revealed that THBS1 in AMϕ-derived exosomes interacted with OTUD5 in endothelial cells, leading to increased GPX4 ubiquitination. OTUD5, a cysteine protease and key member of the OTU deubiquitinase family, consists of 571 amino acids and contains two conserved domains: the OTU domain and the ubiquitin-interacting motif domain [52, 53]. OTUD5 mutations leading to abnormal deubiquitination can cause degradation defects in specific chromatin regulators, resulting in DNA damage [54]. The accumulation of 4-HNE in ischemia–reperfusion-injured cardiomyocytes causes GPX4 degradation through ubiquitination, which can be inhibited by OTUD5 [35]. These findings support the hypothesis that the interaction between THBS1 and OTUD5 mediates increased GPX4 ubiquitination; however, the precise mechanisms require further experimental validation. We also observed that THBS1 regulation not only influenced GPX4 protein levels but also decreased SLC7A11 expression. Thus, further studies are needed to investigate the effects and underlying mechanisms of THBS1 on other ferroptosis-related molecules, such as SLC7A11 and ACSL4.

The above studies confirmed the role of the THBS1-OTUD5-GPX4 axis in regulating ferroptosis and maintaining BBB integrity during CIRI. Building on these findings, we further explored therapeutic strategies targeting this axis. Natural small molecules are valuable resources for drug development because of their structural diversity and bioactivity. We found that salvianolic acid B (SAB) exhibited strong binding affinity for THBS1. SAB, an organic compound derived from *Salvia miltiorrhiza*, exhibits potent antioxidant properties [21]. Previous studies have indicated that SAB alleviates CIRI; however, the underlying mechanisms remain unclear [55]. Molecular docking, molecular dynamics simulations, and CETSA experiments confirmed the effective binding of SAB to THBS1. Furthermore, tail vein injection of SAB significantly alleviated brain injury in MCAO mice. Based on these findings, we hypothesized that SAB's therapeutic effects on CIRI might be associated with its interaction with THBS1, which alters the spatial conformation or post-translational modifications of THBS1, thereby reducing its inhibition of OTUD5, and this hypothesis warrants further investigation. Interestingly, we found that the combination of SAB treatment and macrophagic THBS1 knockdown alleviated brain injury. We propose two possible explanations: (1) SAB treatment may enhance the inhibitory effect of THBS1 knockdown, or [30] the THBS1-OTUD5-GPX4 axis may not be the only pathway through which SAB exerts its effects. However, this observation requires further investigation. In conclusion, our findings indicated that the combination of THBS1 inhibition and SAB treatment may synergistically enhance neuroprotection.

To our knowledge, this is the first study to explore the pathological process by which macrophage-derived exosomal THBS1 promotes GPX4 ubiquitination and degradation through its interaction with OTUD5 in endothelial cells, thereby inducing ferroptosis and exacerbating brain injury during CIRI. However, our study has several limitations. First, we focused only on the impact of macrophages on cerebral vascular endothelial cells during the acute phase of CIRI, without examining long-term neurological deficits, which should be addressed in future studies. Second, AIS is highly age-dependent, with a higher incidence in the elderly. This study followed previous literature, utilizing only 2–3-month-old mice and thereby omitting an investigation of the pathological mechanisms in aged tMCAO mice. Future research will incorporate 18–24-month-old mice, drawing on studies in aged mice models, to validate our findings and elucidate age-related pathological differences. Furthermore, this study focused exclusively on the effects and mechanisms of macrophage-derived exosomal THBS1 on brain vascular endothelial cells, while overlooking other brain vascular cells, such as pericytes and astrocytes, which are essential components of the BBB. Future research should address this limitation and investigate the roles of these cells. Finally, the precise details of the interaction between THBS1 and OTUD5 remain undefined and will be the focus of our future research.

Conclusion

We identified the role of the THBS1-OTUD5-GPX4 axis in CIRI pathology and demonstrated its effect on ferroptosis. Our results showed that during CIRI, macrophage-derived exosomal THBS1 is elevated and transferred to cerebral vascular endothelial cells, where it interacts with OTUD5 to promote GPX4 ubiquitination and degradation. THBS1 knockdown in macrophages significantly improved brain injury. Additionally, SAB effectively bound to THBS1 and significantly alleviated CIRI, thereby amplifying the cerebral protective effects of THBS1 inhibition. These findings deepen our understanding of CIRI and offer novel treatment perspectives.

Abbreviations

AAV	Adeno-associated virus
AIS	Acute ischemic stroke
AMφ-exo	AIS-related-macrophage-derived exosome
BBB	Blood–brain barrier
CETSA	Cellular thermal shift assays
CIRI	Cerebral ischemia/reperfusion injury
CM	Conditioned medium
Fer-1	Ferrostatin-1
GPX4	Glutathione peroxidase 4
GSH	Glutathione
GSSG	Oxidized glutathione
HBMECs	Human brain microvascular endothelial cells
MDA	Malondialdehyde;
Mφ	Macrophage
Mφ-exo	Macrophage-derived exosome
OTUD5	OTU deubiquitinase 5
SAB	Salvianolic acid B
ROS	Reactive oxygen species
THBS1	Thrombospondin-1
tMCAO	Transient middle cerebral artery occlusion

Supplementary Information

The online version contains supplementary material available at https://doi.org/10.1186/s12974-025-03382-x.

Additional file 1: Table S1. Characteristics of the study population. AIS, acute ischemic stroke; HV, healthy volunteers; HDL, high-density lipoprotein; LDL, low-density lipoprotein; APTT, activated partial thromboplastin time; PT, prothrombin time; APTT, activated partial thromboplastin time; AIS, acute ischemic stroke; TIA, transient ischemic attack. Data expressed as the means ± SD, unless indicated otherwise. $P < 0.05$ was considered statistically significant. Table S2. Primer pairs for Quantitative real-time PCR. Table S3. Small interfering RNA sequences. Table S4. The top 15 compounds targeting THBS1. Fig. S1. OGD/R treatment induces a heightened pro-inflammatory response in THP-1 cells. **A** Representative bright field images of THP-1 cells after OGD/R treatment. Scale bar = 100 μm. **B**, **C** Quantification of IL-6 (**B**) and TNF-α (**C**) in THP-1 cells. Data are presented as mean ± SD. $^{**}P < 0.01$, $^{***}P < 0.001$ and $^{****}P < 0.0001$. Fig. S2. Flowchart of exosome enrichment by ultracentrifugation. Fig. S3. THBS1 is highly expressed in OGD/R-treated macrophages. **A** Relative mRNA levels of

THBS1 in THP-1 cells (n = 4). **B** Representative images and statistical graphs of immunofluorescence staining of THBS1 in THP-1 cells (n = 3). Scale bar = 20 μm. **C** Relative mRNA levels of THBS1 in RAW264.7 cells (n = 4). **D** Representative images and statistical graphs of immunofluorescence staining of THBS1 in RAW264.7 cells (n = 3). Scale bar = 20 μm. Data are presented as mean ± SD. *$P < 0.05$, **$P < 0.01$, ***$P < 0.001$, and ****$P < 0.0001$. Fig. S4. Macrophage-derived exosomes are involved in si-ALI through THBS1-induced ferroptosis. **A** Representative immunoblotting for efficiency validation after silencing THBS1 in RAW264.7 cells (n = 4). **B** Transmission electron microscopy (TEM) images of the isolated exosomes from OGD/R-treated RAW264.7 after silencing THBS1. Scale bar = 100 nm. **C** Representative immunoblotting of THBS1 after overexpressing THBS1 in RAW264.7 cells (n = 4). **D** TEM images of the isolated exosomes of OGD/R-treated RAW264.7 after overexpressing THBS1. Scale bar = 100 nm. **E** Relative content of Evans blue in mouse brains (n = 8). **F**, **G** Representative images of Tunel (**F**) and DHE (**G**) staining of mouse brains. Scale bar = 200 μm. **H**, **I** Representative immunoblotting and quantification of barrier-associated proteins (ZO-1, Occludin and Claudin5) and GPX4 proteins in mouse brains (n = 3). Data are presented as mean ± SD. *$P < 0.05$, **$P < 0.01$, ***$P < 0.001$, and ****$P < 0.0001$. Fig. S5. Validation of the biosafety and efficiency of macrophage-specific knockdown of THBS1 in mice. **A** Representative HE-staining images of the brains from mice treated with AAV-NC or AAV-Thbs1. Scale bar = 50 μm. **B** Representative images of DAPI/F4/80/THBS1 immunofluorescence staining in mouse brains. Scale bar = 100 μm. Fig. S6. THBS1 does not directly interact with GPX4. **A**, **B** Representative images of co-immunoprecipitations used to assess the binding between THBS1 and GPX4.

Acknowledgements
We express our gratitude to the staff of the Key Laboratory of Anesthesiology and Intensive Care Research of Heilongjiang Province and the Key Laboratory of Myocardial Ischemia for their assistance. We also thank BioRender.com for providing the tool used to create the experimental design diagram.

Author contributions
CL and HJX conceived and supervised the study. CL, HJS, ZXL and ZYS carried out the animal and cellular experiments. CLL and GMC assisted with imaging experiments. ZXM and HC recruited the patients and collected clinical samples. CL, HJS and ZXL analyzed the data. CL and HJX wrote and edited the manuscript. All authors have read and approved the final manuscript.

Funding
This study was supported by the Second Affiliated Hospital of Harbin Medical University.

Availability of data and materials
The data that support the findings of this study are available from the corresponding author upon reasonable request.

Declarations

Ethics approval and consent to participate
The animal study was carried out by a protocol approved by the Animal Experiment Center of the Second Affiliated Hospital of Harbin Medical University. The experimental protocol was approved by the Ethics Committee (Approval No.: SYDW2021-086). The clinical work has been carried out in accordance with the Code of Ethics of the World Medical Association (Declaration of Helsinki), approved by the Ethics Committee of the Second Affiliated Hospital of Harbin Medical University (Approval No. YJSKY2022-135).

Competing interests
The authors declare no competing interests.

Author details
[1]Department of Anesthesiology, Harbin Medical University Cancer Hospital, Harbin 150081, People's Republic of China. [2]The Key Laboratory of Anesthesiology and Intensive Care Research of Heilongjiang Province, Harbin 150001, People's Republic of China. [3]The Key Laboratory of Myocardial Ischemia Organization, Chinese Ministry of Education, Harbin 150001, People's Republic of China. [4]State Key Laboratory of Frigid Zone Cardiovascular Diseases, Harbin 150001, People's Republic of China. [5]Department of Anesthesiology, Second Affiliated Hospital of Harbin Medical University, Harbin 150001, People's Republic of China. [6]Department of Anesthesiology, Fourth Affiliated Hospital of Harbin Medical University, 37 Yiyuan Road, Harbin 150001, People's Republic of China. [7]Department of Anesthesiology, First Affiliated Hospital of Harbin Medical University, 199 Dazhi Road, Harbin 150001, People's Republic of China.

Received: 31 October 2024 Accepted: 17 February 2025
Published online: 24 February 2025

References

1. Iadecola C, Anrather J. Stroke research at a crossroad: asking the brain for directions. Nat Neurosci. 2011;14:1363–8.
2. Sacco RL, Kasner SE, Broderick JP, Caplan LR, Connors JJ, Culebras A, et al. An updated definition of stroke for the 21st century: a statement for healthcare professionals from the American heart association/American stroke association. Stroke. 2013;44:2064–89.
3. Nitzsche A, Poittevin M, Benarab A, Bonnin P, Faraco G, Uchida H, et al. Endothelial S1P(1) signaling counteracts infarct expansion in ischemic stroke. Circ Res. 2021;128:363–82.
4. Shuaib A, Butcher K, Mohammad AA, Saqqur M, Liebeskind DS. Collateral blood vessels in acute ischaemic stroke: a potential therapeutic target. Lancet Neurol. 2011;10:909–21.
5. Dreikorn M, Milacic Z, Pavlovic V, Meuth SG, Kleinschnitz C, Kraft P. Immunotherapy of experimental and human stroke with agents approved for multiple sclerosis: a systematic review. Ther Adv Neurol Disord. 2018;11:1756286418770626.
6. Yang WS, Stockwell BR. Synthetic lethal screening identifies compounds activating iron-dependent, nonapoptotic cell death in oncogenic-RAS-harboring cancer cells. Chem Biol. 2008;15:234–45.
7. Dixon SJ, Lemberg KM, Lamprecht MR, Skouta R, Zaitsev EM, Gleason CE, et al. Ferroptosis: an iron-dependent form of nonapoptotic cell death. Cell. 2012;149:1060–72.
8. Liu Y, Wan Y, Jiang Y, Zhang L, Cheng W. GPX4: the hub of lipid oxidation, ferroptosis, disease and treatment. Biochim Biophys Acta Rev Cancer. 2023;1878: 188890.
9. Xie Y, Kang R, Klionsky DJ, Tang D. GPX4 in cell death, autophagy, and disease. Autophagy. 2023;19:2621–38.
10. Zheng D, Liu J, Piao H, Zhu Z, Wei R, Liu K. ROS-triggered endothelial cell death mechanisms: focus on pyroptosis, parthanatos, and ferroptosis. Front Immunol. 2022;13:1039241.
11. Liu C, Liu E, Li Z, Li W, Jin J, Sui H, et al. Danlou tablet attenuates ischemic stroke injury and blood-brain barrier damage by inhibiting ferroptosis. J Ethnopharmacol. 2024;322: 117657.
12. Abdul Y, Li W, Ward R, Abdelsaid M, Hafez S, Dong G, et al. Deferoxamine treatment prevents post-stroke vasoregression and neurovascular unit remodeling leading to improved functional outcomes in type 2 male diabetic rats: role of endothelial ferroptosis. Transl Stroke Res. 2021;12:615–30.
13. Fu C, Wu Y, Liu S, Luo C, Lu Y, Liu M, et al. Rehmannioside A improves cognitive impairment and alleviates ferroptosis via activating PI3K/AKT/Nrf2 and SLC7A11/GPX4 signaling pathway after ischemia. J Ethnopharmacol. 2022;289: 115021.
14. Wu R, Gao W, Yao K, Ge J. Roles of exosomes derived from immune cells in cardiovascular diseases. Front Immunol. 2019;10:648.
15. Herisson F, Frodermann V, Courties G, Rohde D, Sun Y, Vandoorne K, et al. Direct vascular channels connect skull bone marrow and the brain surface enabling myeloid cell migration. Nat Neurosci. 2018;21:1209–17.
16. Liu S, Chen J, Shi J, Zhou W, Wang L, Fang W, et al. M1-like macrophage-derived exosomes suppress angiogenesis and exacerbate cardiac dysfunction in a myocardial infarction microenvironment. Basic Res Cardiol. 2020;115:22.
17. Ge X, Tang P, Rong Y, Jiang D, Lu X, Ji C, et al. Exosomal miR-155 from M1-polarized macrophages promotes EndoMT and impairs mitochondrial function via activating NF-κB signaling pathway in vascular

endothelial cells after traumatic spinal cord injury. Redox Biol. 2021;41: 101932.
18. Wang W, Zhu L, Li H, Ren W, Zhuo R, Feng C, et al. Alveolar macrophage-derived exosomal tRF-22-8BWS7K092 activates Hippo signaling pathway to induce ferroptosis in acute lung injury. Int Immunopharmacol. 2022;107: 108690.
19. Wang D, Qiu G, Zhu X, Wang Q, Zhu C, Fang C, et al. Macrophage-inherited exosome excise tumor immunosuppression to expedite immune-activated ferroptosis. J Immunother Cancer. 2023;11: e006516.
20. Longa EZ, Weinstein PR, Carlson S, Cummins R. Reversible middle cerebral artery occlusion without craniectomy in rats. Stroke. 1989;20:84–91.
21. Fu Y, Zhou X, Wang L, Fan W, Gao S, Zhang D, et al. Salvianolic acid B attenuates liver fibrosis by targeting Ecm1 and inhibiting hepatocyte ferroptosis. Redox Biol. 2024;69: 103029.
22. Jiao Y, Zhang T, Zhang C, Ji H, Tong X, Xia R, et al. Exosomal miR-30d-5p of neutrophils induces M1 macrophage polarization and primes macrophage pyroptosis in sepsis-related acute lung injury. Crit Care. 2021;25:356.
23. Gong T, Zhang X, Peng Z, Ye Y, Liu R, Yang Y, et al. Macrophage-derived exosomal aminopeptidase N aggravates sepsis-induced acute lung injury by regulating necroptosis of lung epithelial cell. Commun Biol. 2022;5:543.
24. Zheng Z, Li C, Shao G, Li J, Xu K, Zhao Z, et al. Hippo-YAP/MCP-1 mediated tubular maladaptive repair promote inflammation in renal failed recovery after ischemic AKI. Cell Death Dis. 2021;12:754.
25. Bouet V, Boulouard M, Toutain J, Divoux D, Bernaudin M, Schumann-Bard P, et al. The adhesive removal test: a sensitive method to assess sensorimotor deficits in mice. Nat Protoc. 2009;4:1560–4.
26. Qu M, Zhao J, Zhao Y, Sun J, Liu L, Wei L, et al. Vascular protection and regenerative effects of intranasal DL-3-N-butylphthalide treatment after ischaemic stroke in mice. Stroke Vasc Neurol. 2021;6:74–9.
27. Yu SP, Tung JK, Wei ZZ, Chen D, Berglund K, Zhong W, et al. Optochemogenetic stimulation of transplanted iPS-NPCs enhances neuronal repair and functional recovery after ischemic stroke. J Neurosci. 2019;39:6571–94.
28. Edelmann MJ, Iphöfer A, Akutsu M, Altun M, di Gleria K, Kramer HB, et al. Structural basis and specificity of human otubain 1-mediated deubiquitination. Biochem J. 2009;418:379–90.
29. Wang W, Li Y, Zhang Y, Ye T, Wang K, Li S, et al. SIRT1 mediates the inhibitory effect of dapagliflozin on EndMT by inhibiting the acetylation of endothelium Notch1. Cardiovasc Diabetol. 2023;22:331.
30. Fowler AA 3rd, Truwit JD, Hite RD, Morris PE, DeWilde C, Priday A, et al. Effect of Vitamin C infusion on organ failure and biomarkers of inflammation and vascular injury in patients with sepsis and severe acute respiratory failure: the CITRIS-ALI randomized clinical trial. JAMA. 2019;322:1261–70.
31. Van Der Spoel D, Lindahl E, Hess B, Groenhof G, Mark AE, Berendsen HJ. GROMACS: fast, flexible, and free. J Comput Chem. 2005;26:1701–18.
32. Abraham MJ, Murtola T, Schulz R, Páll S, Smith JC, Hess B, et al. GROMACS: high performance molecular simulations through multi-level parallelism from laptops to supercomputers. SoftwareX. 2015;1–2:19–25.
33. Yao Y, Zhang X, Xu J, Gao F, Wu Y, Cui X, et al. circ_014260/miR-384/THBS1 aggravates spinal cord injury in rats by promoting neuronal apoptosis and endoplasmic reticulum stress. Am J Transl Res. 2022;14:518–33.
34. Guo A, Wang W, Shi H, Wang J, Liu T. Identification of Hub genes and pathways in a rat model of renal ischemia-reperfusion injury using bioinformatics analysis of the gene expression omnibus (GEO) dataset and integration of gene expression profiles. Med Sci Monit. 2019;25:8403–11.
35. Liu L, Pang J, Qin D, Li R, Zou D, Chi K, et al. Deubiquitinase OTUD5 as a novel protector against 4-HNE-triggered ferroptosis in myocardial ischemia/reperfusion injury. Adv Sci. 2023;10: e2301852.
36. Otani T, Furuse M. Tight junction structure and function revisited. Trends Cell Biol. 2020;30:805–17.
37. Keaney J, Campbell M. The dynamic blood-brain barrier. FEBS J. 2015;282:4067–79.
38. Kono H, Rock KL. How dying cells alert the immune system to danger. Nat Rev Immunol. 2008;8:279–89.
39. Jayaraj RL, Azimullah S, Beiram R, Jalal FY, Rosenberg GA. Neuroinflammation: friend and foe for ischemic stroke. J Neuroinflammation. 2019;16:142.
40. Xu X, Gao W, Li L, Hao J, Yang B, Wang T, et al. Annexin A1 protects against cerebral ischemia-reperfusion injury by modulating microglia/macrophage polarization via FPR2/ALX-dependent AMPK-mTOR pathway. J Neuroinflammation. 2021;18:119.
41. Stockwell BR, Friedmann Angeli JP, Bayir H, Bush AI, Conrad M, Dixon SJ, et al. Ferroptosis: a regulated cell death nexus linking metabolism, redox biology, and disease. Cell. 2017;171:273–85.
42. Cui Y, Zhang Y, Zhao X, Shao L, Liu G, Sun C, et al. ACSL4 exacerbates ischemic stroke by promoting ferroptosis-induced brain injury and neuroinflammation. Brain Behav Immun. 2021;93:312–21.
43. Vanhoutte D, Schips TG, Vo A, Grimes KM, Baldwin TA, Brody MJ, et al. Thbs1 induces lethal cardiac atrophy through PERK-ATF4 regulated autophagy. Nat Commun. 2021;12:3928.
44. Xiao M, Zhang J, Chen W, Chen W. M1-like tumor-associated macrophages activated by exosome-transferred THBS1 promote malignant migration in oral squamous cell carcinoma. J Exp Clin Cancer Res. 2018;37:143.
45. Lin TN, Kim GM, Chen JJ, Cheung WM, He YY, Hsu CY. Differential regulation of thrombospondin-1 and thrombospondin-2 after focal cerebral ischemia/reperfusion. Stroke. 2003;34:177–86.
46. Tyzack GE, Sitnikov S, Barson D, Adams-Carr KL, Lau NK, Kwok JC, et al. Astrocyte response to motor neuron injury promotes structural synaptic plasticity via STAT3-regulated TSP-1 expression. Nat Commun. 2014;5:4294.
47. Ursini F, Maiorino M. Lipid peroxidation and ferroptosis: The role of GSH and GPx4. Free Radic Biol Med. 2020;152:175–85.
48. Wang H, You X, Wang J, Chen X, Gao Y, Wang M, et al. MFSD7C protects hemolysis-induced lung impairments by inhibiting ferroptosis. Nat Commun. 2024;15:8226.
49. Dong K, Wei R, Jin T, Zhang M, Shen J, Xiang H, et al. HOIP modulates the stability of GPx4 by linear ubiquitination. Proc Natl Acad Sci USA. 2022;119: e2214227119.
50. Ding Y, Chen X, Liu C, Ge W, Wang Q, Hao X, et al. Identification of a small molecule as inducer of ferroptosis and apoptosis through ubiquitination of GPX4 in triple negative breast cancer cells. J Hematol Oncol. 2021;14:19.
51. Zhang W, Jiang B, Liu Y, Xu L, Wan M. Bufotalin induces ferroptosis in non-small cell lung cancer cells by facilitating the ubiquitination and degradation of GPX4. Free Radic Biol Med. 2022;180:75–84.
52. Mevissen TET, Komander D. Mechanisms of deubiquitinase specificity and regulation. Annu Rev Biochem. 2017;86:159–92.
53. Kim JG, Shin HC, Seo T, Nawale L, Han G, Kim BY, et al. Signaling pathways regulated by UBR box-containing E3 ligases. Int J Mol Sci. 2021;22:8323.
54. Beck DB, Basar MA, Asmar AJ, Thompson JJ, Oda H, Uehara DT, et al. Linkage-specific deubiquitylation by OTUD5 defines an embryonic pathway intolerant to genomic variation. Sci Adv. 2021;7:eabe2116.
55. Guo H, Zhang Z, Gu T, Yu D, Shi Y, Gao Z, et al. Astrocytic glycogen mobilization participates in salvianolic acid B-mediated neuroprotection against reperfusion injury after ischemic stroke. Exp Neurol. 2022;349: 113966.

Publisher's Note